

# Micropulsed Plasma Thrusters for Attitude Control of a Low-Earth-Orbiting CubeSat

Nikolaos A. Gatsonis,<sup>\*</sup> Ye Lu,<sup>†</sup> John Blandino,<sup>‡</sup> and Michael A. Demetriou<sup>§</sup>

Worcester Polytechnic Institute, Worcester, Massachusetts 01609

and

Nicholas Paschalidis<sup>¶</sup>

NASA Goddard Space Flight Center, Greenbelt, Maryland 20771

DOI: 10.2514/1.A33345

This study presents a 3-Unit CubeSat design with commercial-off-the-shelf hardware, Teflon®-fueled micropulsed plasma thrusters, and an attitude determination and control approach. The micropulsed plasma thruster is sized by the impulse bit and pulse frequency required for continuous compensation of expected maximum disturbance torques at altitudes between 400 and 1000 km, as well as to perform stabilization of up to 20 deg/s and slew maneuvers of up to 180 deg. The study involves realistic power constraints anticipated on the 3-Unit CubeSat. Attitude estimation is implemented using the  $q$  method for static attitude determination of the quaternion using pairs of the spacecraft–sun and magnetic-field vectors. The quaternion estimate and the gyroscope measurements are used with an extended Kalman filter to obtain the attitude estimates. Proportional-derivative control algorithms use the static attitude estimates in order to calculate the torque required to compensate for the disturbance torques and to achieve specified stabilization and slewing maneuvers or combinations. The controller includes a thruster-allocation method, which determines the optimal utilization of the available thrusters and introduces redundancy in case of failure. Simulation results are presented for a 3-Unit CubeSat under detumbling, pointing, and pointing and spinning scenarios, as well as comparisons between the thruster-allocation and the paired-firing methods under thruster failure.

## Nomenclature

$A$	=	attitude matrix
$A$	=	surface area, m <sup>2</sup>
$A_s$	=	surface area exposed to the sun, m <sup>2</sup>
$C_D$	=	drag coefficient
$c$	=	speed of light, $3 \times 10^8$ m · s <sup>-1</sup>
$c_g$	=	location of center of gravity, m
$c_{pa}$	=	location of center of aerodynamic pressure
$c_{ps}$	=	location of center of solar pressure
$D$	=	residual magnetic dipole moment, A · m <sup>2</sup>
$D_C$	=	duty cycle
$F$	=	thruster force, N
$F_s$	=	solar constant, 1367 W · m <sup>-2</sup>
$f_P$	=	pulse frequency of the thruster, s <sup>-1</sup>
$g$	=	mean anomaly of the sun, deg
$H_{\text{cdt}}$	=	angular momentum accumulated due to constant disturbance torques, N · m · s
$H_{\text{sl}}$	=	angular momentum required for a 180 deg slew maneuver,
$H_{\text{st}}$	=	angular momentum required for a finite angular velocity change, N · m · s
$h$	=	angular momentum vector in the inertial frame, N · m · s

$I$	=	moment of inertia, kg · m <sup>2</sup>
$I$	=	inertia matrix, kg · m <sup>2</sup>
$I_{\text{bit}}$	=	impulse bit of micropulsed plasma thruster, $\mu\text{N} \cdot \text{s}$
$i$	=	angle of incidence of the sun relative to CubeSat's $X$ axis in body reference frame, deg
$L$	=	mean longitude of the sun, deg
$M$	=	magnetic moment of the Earth, $7.95 \times 10^{15}$ A · m <sup>2</sup>
$M_c$	=	mass of the CubeSat, kg
$N_p$	=	number of pulses
$n_i$	=	unit vector in the thruster force direction
$P$	=	period of the periodic disturbance torques, s
$q$	=	quaternion
$q_{\text{des}}$	=	desired quaternion
$q_r$	=	reflectance factor
$r$	=	orbit radius measured from the center of Earth to the center of mass of satellite, m
$r_C$	=	position vector of the CubeSat from the Earth's center, m
$r_{\text{com}}$	=	position vector of the center of mass from the geometric center, m
$r_{\text{eff},i}$	=	position vector from the center of mass to the equivalent point of thrust application, m
$r_i$	=	position vector of thruster from the geometric center, m
$r_s$	=	distance of the sun from the Earth's center, astronomical unit
$s$	=	thruster moment arm, m
$T_a$	=	disturbance torque from atmospheric drag, $\mu\text{N} \cdot \text{m}$
$T_C$	=	control torque output vector, $\mu\text{N} \cdot \text{m}$
$T_D$	=	disturbance torque vector, $\mu\text{N} \cdot \text{m}$
$T_{\text{Dist},B}$	=	total disturbance torque vector in body reference frame, $\mu\text{N} \cdot \text{m}$
$T_g$	=	disturbance torque from gravity gradient, $\mu\text{N} \cdot \text{m}$
$T_m$	=	disturbance torque from magnetic field, $\mu\text{N} \cdot \text{m}$
$T_{\text{sp}}$	=	disturbance torque from solar radiation, $\mu\text{N} \cdot \text{m}$
$t$	=	firing (or thrust) time, s
$t_p$	=	time between two consecutive pulses, s
$t_P$	=	duration between two consecutive pulses, s
$V$	=	scalar potential in International Geomagnetic Reference Field model
$1U$	=	1 standard Cubesat Unit, 0.1 m × 0.1 m × 0.1 m
$v$	=	velocity of the satellite, m · s <sup>-1</sup>

Received 6 May 2015; revision received 2 September 2015; accepted for publication 3 September 2015; published online 11 January 2016. Copyright © 2015 by Nikolaos Gatsonis, John Blandino, and Michael Demetriou. Published by the American Institute of Aeronautics and Astronautics, Inc., with permission. Copies of this paper may be made for personal or internal use, on condition that the copier pay the \$10.00 per-copy fee to the Copyright Clearance Center, Inc., 222 Rosewood Drive, Danvers, MA 01923; include the code 1533-6794/15 and \$10.00 in correspondence with the CCC.

<sup>\*</sup>Professor, Aerospace Engineering Program, 100 Institute Road. Associate Fellow AIAA.

<sup>†</sup>Graduate Student, Aerospace Engineering Program, 100 Institute Road. Student Member AIAA.

<sup>‡</sup>Associate Professor, Aerospace Engineering Program, 100 Institute Road. Associate Fellow AIAA.

<sup>§</sup>Professor, Aerospace Engineering Program, 100 Institute Road. Senior Member AIAA.

<sup>¶</sup>Heliophysics Science Division Lead Technologist, 8800 Greenbelt Road.

$\alpha$	=	coasting period during slew maneuver, %
$\Delta t_{\text{cdt}}$	=	arbitrary time during which constant disturbance torque is accumulated, s
$\Delta t_{\text{pdt}}$	=	arbitrary time during which periodic disturbance torque is accumulated, s
$\Delta t_{\text{sl}}$	=	desired time to achieve a 180 deg slew maneuver, s
$\Delta t_{\text{st}}$	=	desired time to achieve a finite angular velocity change, s
$\delta$	=	random error component in impulse bit, $\mu\text{N} \cdot \text{s}$
$\varepsilon$	=	obliquity (axial tilt) of the sun's ecliptic, deg
$\theta$	=	geocentric latitude, deg
$\lambda$	=	ecliptic longitude of the sun, deg
$\mu$	=	Earth's gravity constant, $3.986 \times 10^{14} \text{ m}^3 \cdot \text{s}^{-2}$
$\nu$	=	white noise
$\rho$	=	atmospheric density, $\text{kg} \cdot \text{m}^{-3}$
$\tau_p$	=	duration of a single pulse (i.e., active signal), s
$\varphi$	=	east longitude component of a coordinate, deg
$\boldsymbol{\varphi}$	=	error angle vector in attitude control, deg
$\boldsymbol{\omega}$	=	angular velocity vector, $\text{rad} \cdot \text{s}^{-1}$

### Subscripts

$G$	=	gyroscope
$M$	=	magnetometer
$S$	=	sun sensor
$x$	=	about $X$ axis
$y$	=	about $Y$ axis
$z$	=	about $Z$ axis

### Superscripts

$b$	=	body reference frame
$e$	=	Earth-centered Earth-fixed reference frame
$i$	=	Earth-centered inertial reference frame
$n$	=	north-east-down reference frame

## I. Introduction

CUBESATS have emerged as platforms for various low-Earth-orbit (LEO) applications. Attitude control using propulsion requires the development of propulsive options that are consistent with the physical constraints of CubeSats and provides the required impulse for typical LEO applications while allowing for novel implementation and development of suitable control approaches. A feasibility study is presented in [1], where a 1U module of micro-pulsed plasma thrusters ( $\mu\text{PPTs}$ ) was applied for attitude control of a 3-Unit (3U) CubeSat design with commercial-off-the shelf (COTS) sensors at altitudes between 400 and 100 km. In this study, we further develop the CubeSat and mission design, as well as the  $\mu\text{PPT}$  sizing analysis that, in addition to compensation of disturbance torques, includes stabilization (detumbling, spinning, and despinning) and slew (pointing) maneuvers. We also introduce an attitude determination and estimation method, sensor models, and an improved attitude control approach that includes a thruster-allocation method for robustness in place of the paired firing followed by Gatsonis et al. [1]. The  $\mu\text{PPT}$  design and attitude determination and control (ADC) approach developed in this study can be applied to other nanosatellites (less than 10 kg) at LEO altitudes.

The attitude control of CubeSats can use magnetic torquers, reaction wheels, control moment gyroscopes, or thrusters. Magnetic torquers are very popular due to their low mass, reliability, and efficiency. The downside is that they cannot produce the magnitude of torque required for fast maneuvers with the power available [2,3]. Reaction wheels can produce higher control torque output than magnetic torquers but are more massive, will require more power, and can be less reliable over an extended lifetime due to the rotating wheels [4,5]. Reaction wheels are usually used in combination with magnetic torquers to allow for wheel desaturation [6,7].

Propulsive options for attitude control of CubeSats are an emerging area, and candidate technologies include cold gas and electric thrusters. The main consideration in implementing propulsion relates to the

limitations on volume, mass, and power available on CubeSats. Cold-gas micropropulsion with a mass of 0.509 kg, a thrust of 55 mN, a specific impulse of 65 s, and a total impulse of 34 N · s was considered for aerodynamic drag compensation on a CubeSat [8]. Delfi-next, a 3U CubeSat launched in 2013, was carrying a cold-gas micro-propulsion system with a thrust of 6 mN and a specific impulse  $I_{\text{sp}}$  of over 30 s to maintain its orbit [9]. The use of a highly miniaturized propulsion system (e.g., cold-gas thruster) to demonstrate relative motion control between two CubeSats was investigated by Sundaramoorthy et al. [10]. A resistojet with a propellant mass of 0.6 kg, a  $I_{\text{sp}}$  of 67–890 s, and a volume of 1U, was considered by Moore et al. [11] for the 2U Rapidprototyped Mems Propulsion And Radiation Test (RAMPART) CubeSat. A propulsion module with eight  $\mu\text{PPTs}$  for yaw, pitch, and roll control was considered by Shaw and Lappas [12] on Surrey Training, Research and Nanosatellite Demonstrator 1 (STRaND-1), which is a 3U CubeSat. The propulsion module has a total mass of 0.34 kg, with each  $\mu\text{PPT}$  producing an impulse bit  $I_{\text{bit}}$  of 0.56  $\mu\text{N} \cdot \text{s}$  and a specific impulse of over 300 s. Due to the limited control authority of this module, the final design excluded thrusters for attitude control; and a cold-gas system was integrated for orbit control only. Clark et al. [13] evaluated the performance requirement of a  $\mu\text{PPT}$  with 0.3U and 150 g mass for drag compensation and orbit maintenance. The University Wuerzburg Experimental (UWE-4) picosatellite is the first to incorporate vacuum arc thrusters for orbit control of a CubeSat. The total propulsion system mass is only 0.2 kg, the impulse bit is 0.01 – 0.1  $\mu\text{N} \cdot \text{s}$ , and the maximum pulse frequency is 20 Hz [14]. Conversano and Wirz [15] have assessed the mission capability of CubeSats using a miniature ion thruster. They showed that, depending on the thruster and propellant available, the delta  $V$  could range from 1000 m/s to over 7000 m/s, enabling low-Earth-orbit inclination changes and even lunar missions.

In this study, we present a 3U CubeSat design with  $\mu\text{PPTs}$  and an ADC approach. The 3U CubeSat design follows the work of Gatsonis et al. [1] but includes an option for fully deployable solar arrays. The  $\mu\text{PPT}$  is sized by the impulse bit and pulse frequency required to provide angular momentum (and rate) for continuous compensation of the maximum expected disturbance torques, stabilization (5, 10, 20 deg/s), and slew (180 deg) maneuvers. The  $\mu\text{PPT}$  is sized using simulation tools developed in a series of pulsed plasma thruster (PPT) investigations in [16–18]. The attitude determination and control method combines established approaches [19–22], and the controller involves a thruster-allocation method that increases the robustness of attitude control in case of thruster failure. Attitude estimation is implemented as a two-step process. During the first step, we follow the  $q$  method for static attitude determination to obtain an estimate of the quaternion using pairs of the spacecraft–sun and magnetic-field vectors: one in the inertial reference frame, and one in the body frame of the CubeSat. During the second step, we use the quaternion estimate and the gyroscope measurements with an extended Kalman filter to obtain the attitude estimates. These estimates are subsequently used in proportional and derivative control algorithms to calculate the torque required to compensate for the disturbance torques and to achieve specified stabilization and slewing maneuvers or combinations. The controller includes a thruster-allocation method that finds the optimal utilization of the available thrusters.

In Sec. II, we introduce the CubeSat configuration and coordinate systems. In Sec. III, we provide an estimate of worst-case disturbance torques, determine the required impulse bit and pulse frequency of the  $\mu\text{PPT}$ , and present the design of propulsion module. In Sec. IV, we introduce the attitude dynamics; the attitude determination method; the sensor and reference models, a description of attitude estimation; and the attitude control scheme, which includes an optimal thruster allocation. In Sec. V, we present simulation results for detumbling after insertion, pointing, and pointing and spinning scenarios in the presence of disturbance torques, as well as a comparison between the thruster-allocation and paired-firing methods of [1]. Finally, in Sec. VI, we present conclusions and discuss the impact of this study.

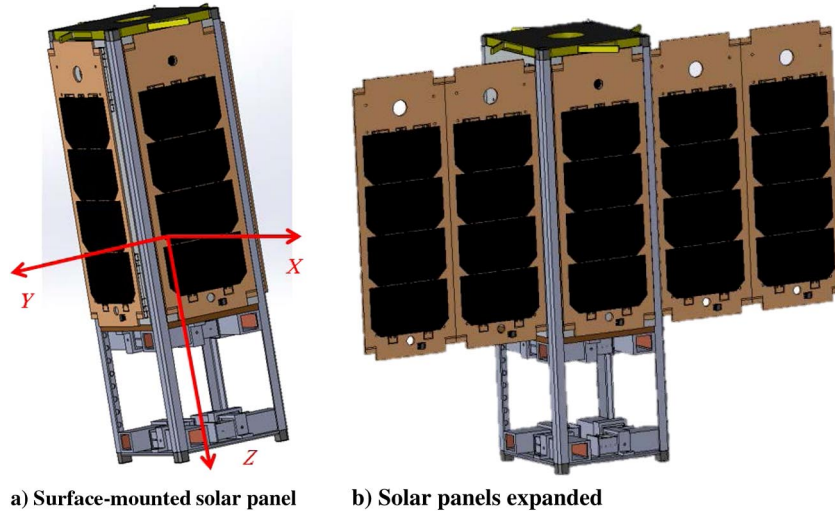


Fig. 1 3U CubeSat with the  $\mu$ PPT module located in the bottom 1U. a) Surface mounted solar panel; b) Solar panels expanded.

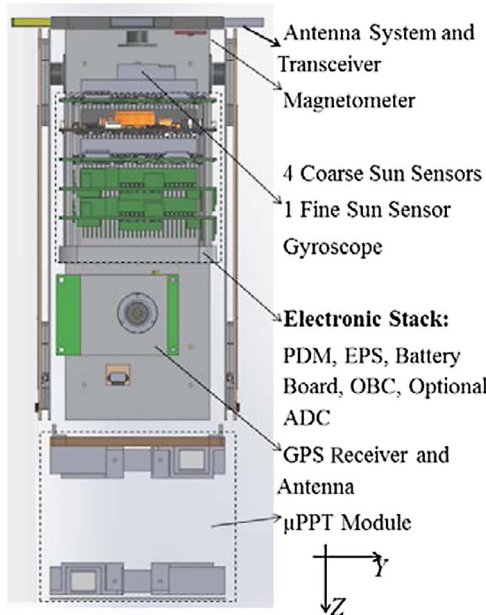


Fig. 2 U CubeSat with sun sensors placed on  $+Y$ ,  $-Y$ ,  $-X$ ,  $+X$ , and  $-Z$  faces.

## II. CubeSat Design

### A. CubeSat Configurations

The baseline configuration of the 3U CubeSat considered is shown in Fig. 1 and is a result of a series of design studies [23–26]. The CubeSat is equipped with a magnetometer, a gyroscope, a Global Positioning System receiver, and five sun sensors, as shown in Fig. 2 for attitude determination. The CubeSat has an electrical power subsystem, a power distribution module, a battery board, and an onboard computer. The bottom 1U is devoted to the thruster module with eight  $\mu$ PPTs for attitude control. Two options for ADC are shown in Fig. 1: one with surface-mounted solar panels, and the second with deployable solar panels, where the latter will be investigated in this work.

The  $\mu$ PPT module shown in Fig. 1 is designed to provide three-axis control for a 3U CubeSat. It consists of eight rectangular-geometry  $\mu$ PPTs arranged in two layers. Each  $\mu$ PPT includes a miniature spark igniter, which creates a conductive path to initiate the primary discharge. This primary discharge has a period of  $\tau_p$ , during which ablation and ionization of Teflon forms a plasma that is accelerated with electromagnetic and gas dynamic forces to produce thrust.

### B. Reference Frames

The design of the CubeSat, sensor modeling, and implementation of the dynamics and attitude control method requires use of five reference frames: the Earth-centered inertial (ECI), the Earth-centered Earth-fixed (ECEF), the body reference frame (BRF), the mission reference frame (MRF), and the north-east-down (NED) frame. The ECI frame, shown in Fig. 3a, is inertial and is best for describing the orbital motion of the satellite. The ECEF shown in Fig. 3b is a rotating frame with reference to a fixed point on the surface of the Earth. It is used by the Global Positioning System. The NED reference frame shown in Fig. 3c is used in the International Geomagnetic Reference Field (IGRF) model. The BRF shown in Fig. 1 has its origin coincident with the center of mass of the CubeSat and is primarily used for describing sensor measurements and actuator output. The  $X$  axis in the BRF shown in Fig. 3a is in the direction of the normal to the solar panels when they are fully deployed (Fig. 3b), and the  $Z$  axis is placed along the minor axis of inertia. The MRF shown in Fig. 3d is mission specific. In this study, where sun pointing is of interest, we define the  $Z$  axis to be oriented along the direction of the sun (or other targets), with the  $Y$  axis orthogonal to the  $Z$  axis and nadir direction.

## III. Thruster Requirements for Disturbance Torques Compensation, Stabilization, and Slew Maneuvers

### A. Angular Momentum Evaluation

The  $\mu$ PPT sizing (impulse bit and pulse frequency) requires evaluation of angular momentum imparted from disturbance torques over a specified time and the evaluation of angular momentum needed for stabilization and slewing maneuvers. We consider four cases of angular momentum: the  $H_{\text{adt}}$  accumulated from maximum constant disturbance torques over a time  $\Delta t_{\text{cdt}}$ ; the  $H_{\text{pdt}}$  accumulated from periodic disturbance torques over time  $\Delta t_{\text{pdt}}$ ; the  $H_{\text{st}}$  required for despinning or spinning up within  $\Delta t_{\text{st}}$ , for a change in angular velocity of  $\Delta\omega$ ; and the  $H_{\text{sl}}$  associated with a 180 deg slew maneuver over time  $\Delta t_{\text{sl}}$  with zero initial and final angular velocities.

CubeSats in LEO experience disturbance torques due to aerodynamic drag, gravity gradient, the magnetic field, and solar radiation [27]. The disturbance torque due to aerodynamic drag is described by

$$T_a = \rho A C_D v^2 (c_{pa} - c_g) / 2 \quad (1)$$

where  $\rho$  is the background atmospheric density,  $A$  is the cross-sectional surface area normal to the velocity vector,  $C_D$  is the drag coefficient,  $v$  is the speed,  $c_{pa}$  is the center of aerodynamic pressure, and  $c_g$  is the center of mass of the CubeSat. The gravitational torque is due to the variation of the gravitational force over the CubeSat. Assuming a spherical mass distribution for the Earth, the gravitational torque is given by [27]

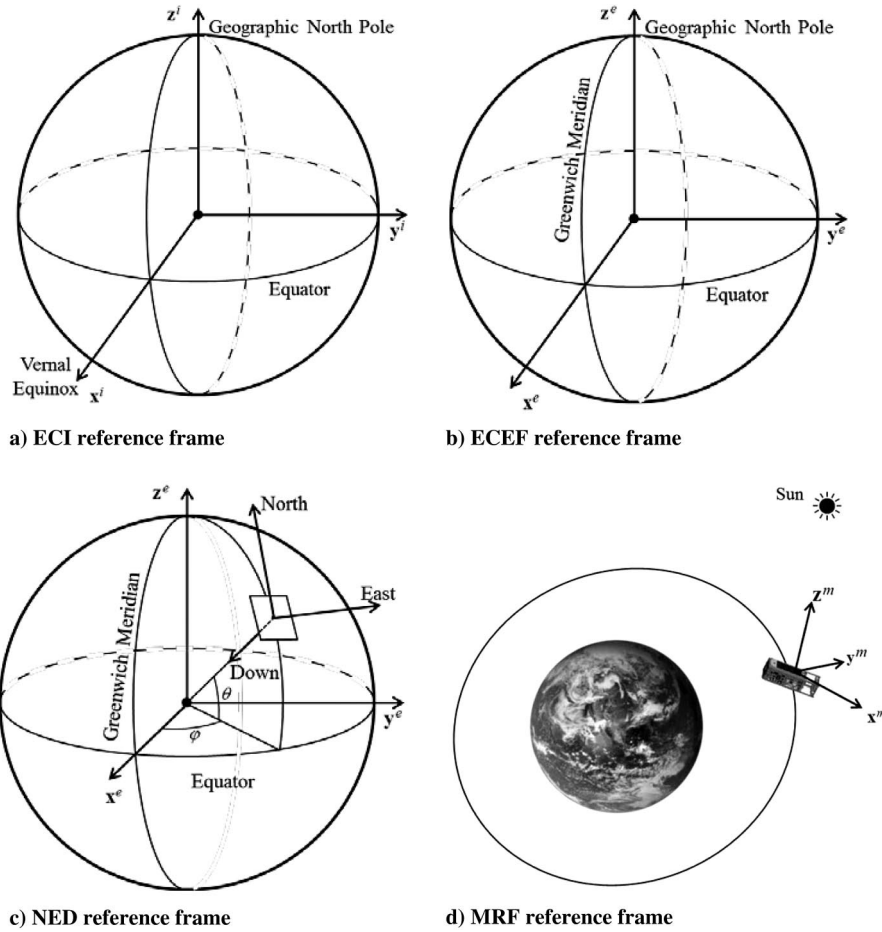


Fig. 3 Reference frames used in the sensor and actuator model for attitude control analysis.

$$T_g = 3\mu|I_z - I_y| \sin(2\beta)/2r^3 \quad (2)$$

where  $\mu = 3.986 \times 10^5 \text{ km}^3 \cdot \text{s}^{-2}$  is the Earth's gravity constant,  $r$  is orbit radius (in kilometers),  $\beta$  is the maximum deviation of the  $Z$  axis (in the BRF) relative to a nadir pointing vector in radians, and  $I_z$  and  $I_y$  are the minor moments of inertia. The solar radiation torque is given by [27]

$$T_{sp} = F_s A_s \cos(i)(1 + q_r)(c_{ps} - c_g)/c \quad (3)$$

where  $F_s = 1367 \text{ W/m}^2$  is the incident solar radiation constant,  $c$  is the speed of light,  $A_s$  is the surface area,  $c_{ps}$  is the location of the center of solar pressure,  $c_g$  is the center of mass,  $q_r$  is the reflectance factor, and  $i$  is the angle of incidence of the sun relative to the  $X$  axis in the BRF ( $i = 0$  if the sunlight is aligned with  $X$  axis). Finally, the magnetic torque from the interaction between the Earth's geomagnetic field and the satellite's residual magnetic dipole moment [27] is given by

$$T_m = D2M/r^3 \quad (4)$$

Table 1 Input parameters for evaluation of disturbance torques of the 3U CubeSat shown in Fig. 1b

Parameter	Value
$C_D$	3
$A$	0.11 m <sup>2</sup>
$c_{pa} - c_g$	0.05 m
$\beta$	30 deg
$I_z - I_y$	0.025 kg · m <sup>2</sup>
$A_s$	0.11 m <sup>2</sup>
$c_{ps} - c_g$	0.05 m
$q_r$	1
$i$	0 deg
$D$	0.004 A · m <sup>2</sup>

where  $M = 7.96 \times 10^{15} \text{ T} \cdot \text{m}^3$  is the magnetic moment of the Earth; and  $D$  is the residual magnetic dipole moment generated by onboard instruments and current-carrying wires and is estimated based on the mass of the CubeSat  $M_c$  as  $D = M_c \times 0.001 \text{ A} \cdot \text{m}^2/\text{kg}$  [20].

For evaluation of the maximum torques, we consider the 3U CubeSat shown in Fig. 1b on a circular orbit with its solar panels fully deployed, velocity  $v = \sqrt{\mu/r}$  in the direction normal to the solar panels, and input parameters as shown in Table 1. The aerodynamic torque is evaluated for maximum and minimum solar activity conditions. Figure 4 shows the disturbance torques as a function of altitude. At altitudes above 500 km, the maximum disturbances are primarily due to solar pressure and magnetic field, whereas at altitudes below 400 km, the aerodynamic torque becomes dominant. At an altitude of 400 km, the maximum disturbance torque is  $T^{\max} = 6 \times 10^{-6} \text{ N} \cdot \text{m}$ .

The maximum constant angular momentum accumulated over an arbitrary time  $\Delta t_{\text{cdt}}$  due the maximum disturbance torque  $T^{\max}$  is

$$H_{\text{cdt}} = T^{\max} \Delta t_{\text{cdt}} \quad (5)$$

The periodic angular momentum accumulated over time  $\Delta t_{\text{cdt}}$  due to disturbance torques with period  $P$  is

$$H_{\text{pdt}} = \int_0^{\Delta t_{\text{pdt}}} |T(t)| dt = \int_0^{\Delta t_{\text{pdt}}} T^{\max} \cos\left(\frac{2\pi}{P}t\right) dt \quad (6)$$

The absolute value sign is used to calculate the accumulated angular momentum magnitude, and the disturbance torque is continuously compensated over the time period of interest. Consider a time such that  $\Delta t_{\text{pdt}}$  is an integer multiple of  $P$ ; then, Eq. (6) can be rewritten as

$$H_{\text{pdt}} = \frac{\Delta t_{\text{pdt}}}{P} 2 \int_0^{P/2} T^{\max} \cos\left(\frac{2\pi}{P}t\right) dt = T^{\max} \frac{\Delta t_{\text{pdt}}}{\pi} \quad (7)$$

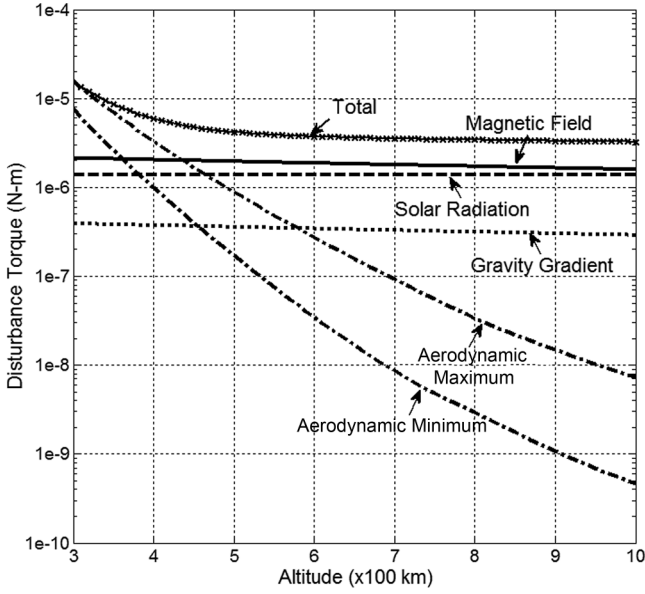


Fig. 4 Disturbance torques on the 3U CubeSat shown in Fig. 1b at altitudes from 300 to 1000 km.

The angular momentum required for stabilization (despinning) or spinning up with a change in angular velocity of  $\Delta\omega$  is

$$H_{st} = I|\Delta\omega| \quad (8)$$

For slow maneuvers, we assume that  $\omega_i = \omega_f = 0$  deg/s,  $\Delta t_{sl}$  is the required slow time, and the idle period (i.e., the amount of time when the thrust is not applied) is  $\alpha\Delta t_{sl}$ , as shown in Fig. 5.

The angular velocity  $\omega_{max}$  needed is given by

$$\begin{aligned} \Delta\theta &= \alpha \cdot \Delta t_{sl} \cdot \omega_{max} + (1 - \alpha) \cdot \Delta t_{sl} \cdot \omega_{max}/2 \\ \omega_{max} &= 2\Delta\theta / (1 + \alpha)\Delta t_{sl} \end{aligned} \quad (9)$$

Then, the angular momentum required for such a slow maneuver is

$$H_{sl} = I(|\omega_{max} - \omega_0| + |\omega_{max} - \omega_f|) = 4I\Delta\theta / (1 + \alpha)\Delta t_{sl} \quad (10)$$

### B. Impulse Bit and Pulse Frequency Requirements

The  $\mu$ PPT considered in this investigation has a rectangular geometry and uses solid Teflon as a propellant. Each pulse shown in Fig. 6 has a duration  $\tau_p$  that is assumed to be equal to the duration of the primary capacitor discharge. The firing (or thrust or pulse) period is  $t_p$ , the pulse frequency is  $f_p = t_p^{-1}$ , and the duty cycle is expressed as the percentage of one period in which thrust is produced  $D_C = (\tau_p/t_p)100\%$ . The duration of  $N_p$  pulses (i.e., total on time when the thrust is produced), is

$$\tau = N_p \cdot \tau_p \quad (11)$$

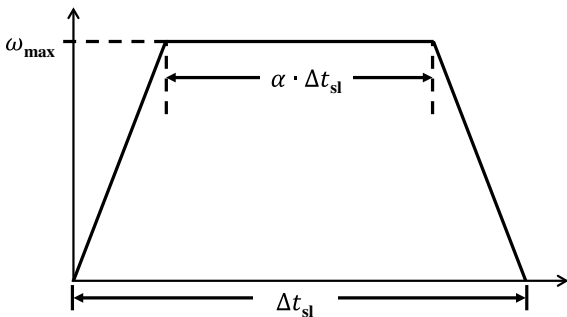


Fig. 5 Illustration showing angular velocity vs time for slow maneuver. Also shown is idle period with constant angular velocity.

and the total firing (or thrust) time, which includes the on time and off time, is

$$t = N_p \cdot t_p = N_p / f_p \quad (12)$$

For thruster sizing purposes, we need to determine the required impulse bit  $I_{bit}$  and pulse frequency  $f_p$  for the  $\mu$ PPT. For an angular momentum  $H$  to be delivered by a thruster with moment arm of  $s$ , the number of pulses per thruster is

$$N_p = H / n \cdot I_{bit} \cdot s \quad (13)$$

where  $n$  is the number of thrusters in one of the six directions (positive  $x$ ,  $y$ , and  $z$ ; and negative  $x$ ,  $y$ , and  $z$  directions). The thruster has the property of providing a unilateral control reaction, which means that the thruster providing torque in the positive  $x$  direction can only produce torque in the positive  $x$  direction. For attitude control, at least one thruster is needed for one of the six directions, and six thrusters are required to maintain full control over three axes. Note that thrust forces are not acting as balanced couples, and the resulting translational motion will result in a velocity change on the order of  $10^{-3}$  ms<sup>-1</sup>/day with a corresponding displacement on the order of tens of meters per day, if acting in the same direction. Because of their small magnitude in comparison to the nominal orbital parameters, such translational motions are neglected.

We can also obtain the required firing time using Eq. (12) and rewrite Eq. (13) as

$$t = H / f_p \cdot n \cdot I_{bit} \cdot s \quad (14)$$

By introducing the average angular momentum rate  $\dot{H} = H/t$ , the preceding equation can be written as

$$f_p \cdot I_{bit} \cdot n \cdot s = \dot{H} \quad (15)$$

which relates the thruster design parameters,  $I_{bit}$  and  $f_p$ , and the CubeSat design characteristics,  $n$  and  $s$ , to the mission requirement  $\dot{H}$  (or  $H$  derived earlier over the desired firing time  $t$ ).

For a constant disturbance torque, if compensation is achieved continuously over a firing time of  $t = \Delta t_{cdt}$ , then

$$\dot{H}_{cdt} = T^{max} \quad (16)$$

For a periodic disturbance torque, if compensation is achieved over a time period of  $t = \Delta t_{pdt}$ , then

$$\dot{H}_{pdt} = T^{max} / \pi \quad (17)$$

For stabilization or spinning up,  $t = \Delta t_{st}$ ; therefore,

$$\dot{H}_{st} = I|\Delta\omega| / \Delta t_{st} \quad (18)$$

For the slow maneuver, the firing time  $t = (1 - \alpha)\Delta t_{sl}$  and

$$\dot{H}_{sl} = 4I\Delta\theta / (1 - \alpha^2)\Delta t_{sl}^2 \quad (19)$$

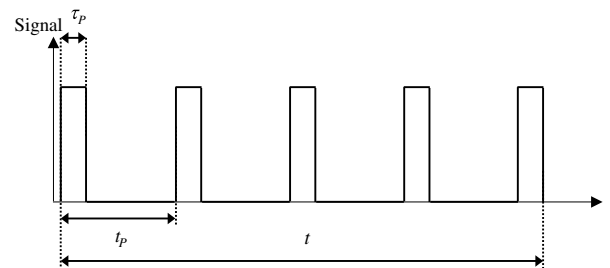


Fig. 6 Diagram representing idealized, thrust vs time profile for a PPT pulse train.

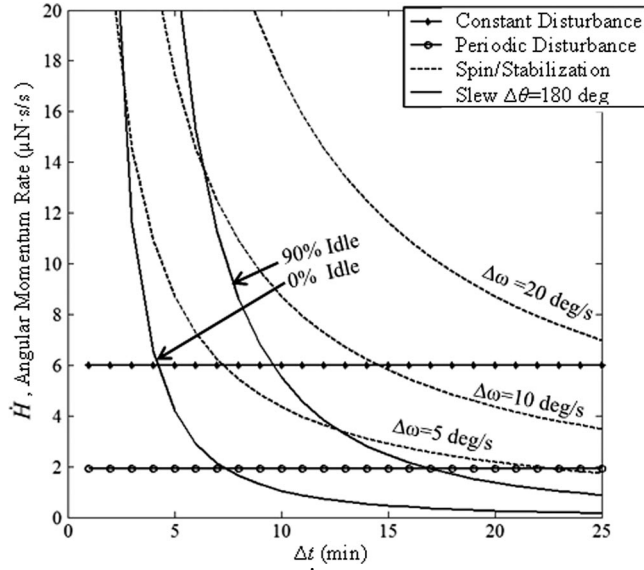


Fig. 7 Angular momentum rate  $\dot{H}$  for maneuvers of a given duration for the 3U Cubesat shown in Fig. 1b.

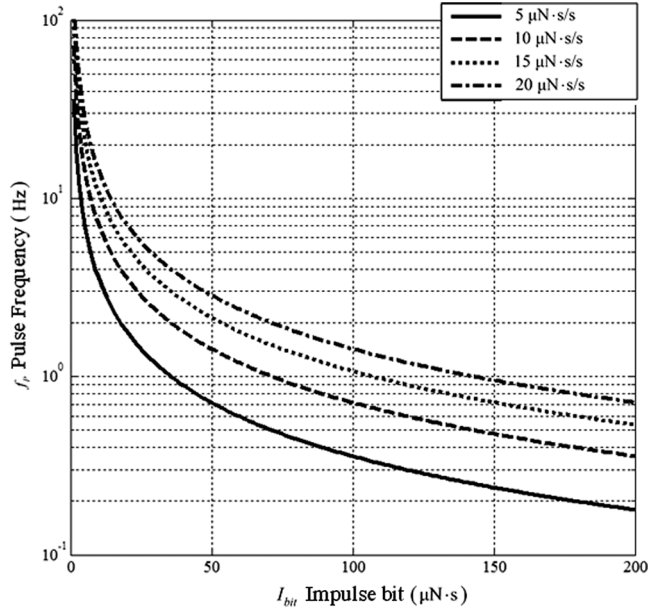


Fig. 8 Required impulse bit and pulse frequency for different angular momentum rates of a 3U CubeSat shown in Fig. 1b.

For a 3U CubeSat with thrusters located as shown in Fig. 1a, the moment arm has values from 3 to 20 cm. We assume that  $s = 0.14$  m and that there is only one  $\mu$ PPT in each of the  $+/-x$ ,  $+/-y$  and  $+/-z$  directions, so  $n = 1$ . For a given maneuver and time duration, the angular momentum rate is found using Eqs. (16–19), and it is plotted in Fig. 7. For the constant and periodic disturbance, the compensation is assumed to be continuous. Then, Eq. (15) is used to provide bounds on the required  $I_{\text{bit}}$  and  $f_p$  of the  $\mu$ PPT, which are plotted in Fig. 8.

### C. Micropulsed Plasma Thruster Design

The rectangular  $\mu$ PPT can be accommodated within the available volume in the 3U CubeSat and is sized to provide the required impulse bit. The propulsion module, consisting of thrusters, fits in a 1U volume of a CubeSat. The design and performance characteristics ( $I_{\text{sp}}$ ,  $I_{\text{bit}}$ ) of the  $\mu$ PPT are derived in an iterative procedure using the performance model of Laperriere et al. [16] in conjunction with the ablation model of Gatsonis et al. [17]. The performance model includes inputs that incorporate several design features of a rectangular  $\mu$ PPT (e.g.,

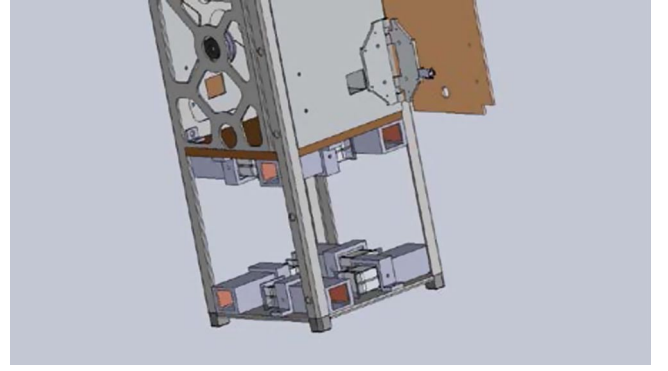


Fig. 9 Bottom 1U of CubeSat showing the thrusters comprising the  $\mu$ PPT module.

geometrical features, discharge time, circuit parameters, and electrical characteristics of the electrodes). The ablation model is used to provide the total mass ablated per pulse, using as inputs the geometrical characteristics of the Teflon bar, pulse duration, and material properties. Using these two models, we designed a  $\mu$ PPT and propulsion module, as shown in Fig. 9. The  $\mu$ PPT is designed with two parallel tungsten-coated copper electrodes, which were housed in a Torlon® casing. This  $\mu$ PPT design can provide an  $I_{\text{bit}}$  between 10 and 80  $\mu\text{N} \cdot \text{s}$ , with input energy below 2 J per pulse, and operates over the range of pulse frequencies  $f_p$  shown in Fig. 8. The  $\mu$ PPT shown in Fig. 9 has an electrode thickness of 0.75 cm, a length of 3.6 cm, a width of 1.25 cm, a channel height of 1.65 cm, and a Teflon bar of about 10 g.

## IV. Attitude Dynamics, Estimation and Control

### A. Attitude Dynamics and Estimation

The 3U CubeSat is modeled as a rigid body, and its attitude dynamics is expressed via Euler's equation in terms of the angular velocity,  $\omega(t) = (\omega_x(t), \omega_y(t), \omega_z(t))$ , the disturbance torques  $T_D(t)$ , the control torque  $T_C(t)$ , and the inertia matrix  $I$  [16]:

$$I\dot{\omega}(t) = [T_C(t) + T_D(t) - (\omega(t) \times I\omega(t))] \quad (20)$$

The differential equation for the quaternion kinematics  $q(t)$  is given by

$$\begin{aligned} \dot{q}(t) &= \frac{1}{2} \Omega(\omega(t)) q(t) \\ &= \frac{1}{2} \begin{bmatrix} 0 & \omega_z(t) & -\omega_y(t) & \omega_x(t) \\ -\omega_z(t) & 0 & \omega_x(t) & \omega_y(t) \\ \omega_y(t) & -\omega_x(t) & 0 & \omega_z(t) \\ -\omega_x(t) & -\omega_y(t) & -\omega_z(t) & 0 \end{bmatrix} q(t) \end{aligned} \quad (21)$$

Attitude estimation is implemented in this study as a two-step process following established approaches [19–22], as shown in Fig. 10. Note that orbital state data are not propagated in this study, so the CubeSat position is preloaded from Systems Tool Kit (STK) simulations [28]. During the first step, we follow the  $q$  method for static attitude determination to obtain an estimate of the quaternion denoted by  $y_q(t)$ . The  $q$  method uses pairs of the spacecraft–sun and the magnetic-field vectors: one in the inertial reference frame, and one in the body frame of the CubeSat. During the second step, we use the quaternion estimate  $y_q(t)$  and the gyroscope measurements denoted by  $y_G^b(t)$  with an extended Kalman filtering (EKF) algorithm to obtain the attitude estimates  $\hat{\omega}(t)$  and  $\hat{q}(t)$  as shown in Fig. 11.

### B. Static Attitude Determination

#### 1. Davenport $q$ Method

The  $q$  method uses two or more sets of noncollinear vectors: one in the inertial reference frame, and one in the body frame of the CubeSat to obtain the direction cosine matrix that relates the two frames. The body-fixed vector  $y^b$  provides the measured directions by the



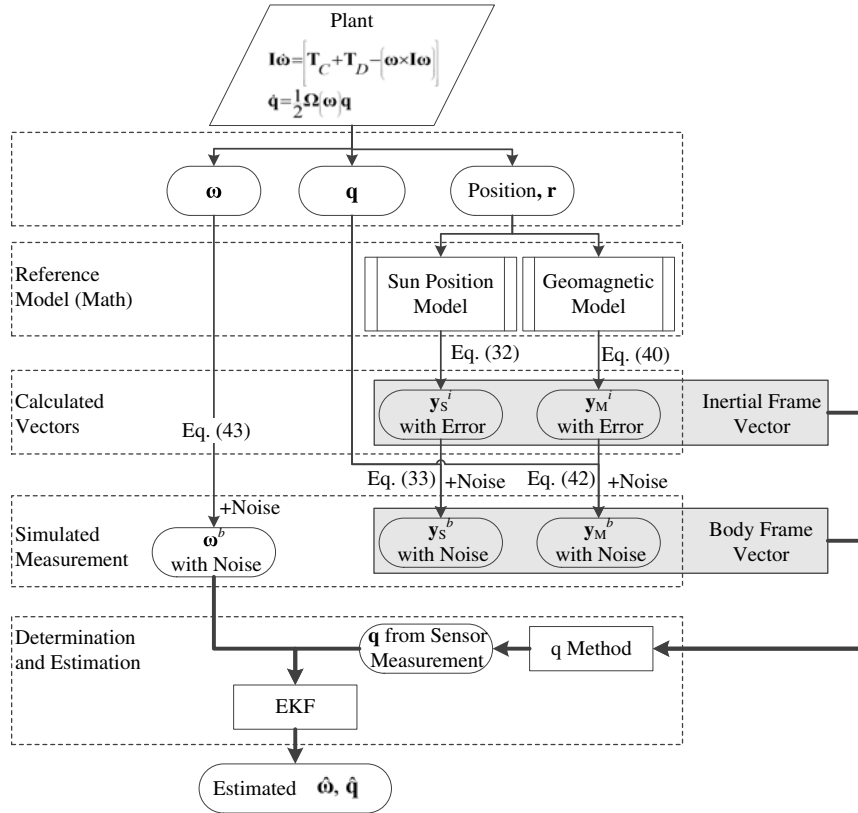


Fig. 10 Flowchart for simulation, determination, and estimation.

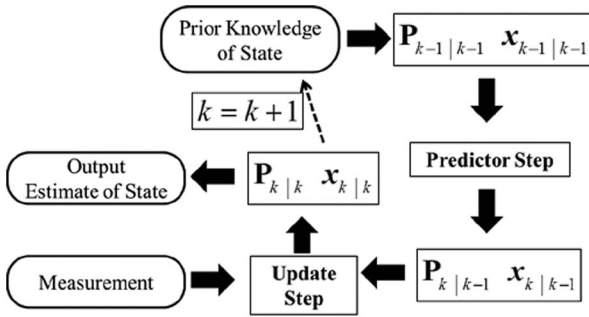


Fig. 11 Outline for extended Kalman filter algorithm.

onboard sensors, and the inertial-frame vector  $\mathbf{y}^i$  provides the directions from a reference (mathematical) model. The two directions are related by the rotational matrix  $\mathbf{A}^{bi}$  from ECI to the BRF such that

$$\mathbf{y}^b = \mathbf{A}^{bi} \mathbf{y}^i + \delta \mathbf{y} \quad (22)$$

where  $\delta \mathbf{y}$  is an error term that denotes errors from both sensor measurements and mathematical models. The attitude matrix  $\mathbf{A}^{bi}$  can be represented as [20]

$$\mathbf{A}^{bi}(\mathbf{q}) = (q_4^2 - \|\mathbf{q}_{1:3}\|^2) \mathbf{I}_{3 \times 3} + 2\mathbf{q}_{1:3} \mathbf{q}_{1:3}^T - 2q_4 [\mathbf{q}_{1:3} \times] \quad (23)$$

where the quaternion  $\mathbf{q} = [q_{1:3}^T \ q_4]^T$ , with  $\mathbf{q}_{1:3}$  as its vector part and  $q_4$  as its scalar component; and  $[\mathbf{q}_{1:3} \times]$  is the cross-product matrix defined by

$$[\mathbf{q}_{1:3} \times] \triangleq \begin{bmatrix} 0 & -q_3 & q_2 \\ q_3 & 0 & -q_1 \\ -q_2 & q_1 & 0 \end{bmatrix} \quad (24)$$

where  $q_i$  is the  $i$ th entry in the vector part  $\mathbf{q}_{1:3}$  of the quaternion. Wahba [29] proposed a constrained least-squares estimation for

finding an orthogonal matrix  $\mathbf{A}^{bi}$  with determinant +1 using  $n$  measurements as

$$\min_{\mathbf{A}^{bi}} \sum_{j=1}^n \|(\mathbf{y}^b)_j - \mathbf{A}^{bi} (\mathbf{y}^i)_j\|^2 \text{ subject to } \det[\mathbf{A}^{bi}] = 1 \quad (25)$$

where  $(\mathbf{y}^b)_j$  and  $(\mathbf{y}^i)_j$ ,  $j = 1, \dots, n$  are the  $n$  unit vectors measured in the body and inertial frame, respectively. The preceding equation can be solved using the  $q$  method with Eq. (23), represented as [20]

$$\frac{1}{2} \sum_{j=1}^n a_j \|(\mathbf{y}^b)_j - \mathbf{A}^{bi} (\mathbf{y}^i)_j\|^2 = 1 - \mathbf{q}^T \mathbf{K} \mathbf{q} \quad (26)$$

where  $\{a_j\}$  are nonnegative weights, assumed for simplicity to be equal to  $1/n$ . The symmetric traceless matrix  $\mathbf{K}$  is evaluated through the set of measured (body-frame) and reference (inertial-frame) vectors

$$\mathbf{K} \triangleq \begin{bmatrix} \mathbf{S} - \text{tr}(\mathbf{D}) \mathbf{I}_{3 \times 3} & \mathbf{N} \\ \mathbf{N}^T & \text{tr}(\mathbf{D}) \end{bmatrix} \quad (27)$$

where

$$\begin{aligned} \mathbf{S} &= \mathbf{D} + \mathbf{D}^T, \\ \mathbf{D} &= \sum_{j=1}^n a_j (\mathbf{y}^b)_j [(\mathbf{y}^i)_j]^T, \\ \mathbf{N} &= \sum_{j=1}^n a_j ((\mathbf{y}^b)_j \times (\mathbf{y}^i)_j) \end{aligned} \quad (28)$$

The optimal quaternion estimate using Davenport's  $q$  method is given by

$$\mathbf{y}_q = \mathbf{q}_{\max} \quad (29)$$

where  $\mathbf{q}_{\max}$  is the normalized eigenvector corresponding to the largest eigenvalue of  $\mathbf{K}$  in Eq. (27).

## 2. Sensors and Reference Models

The reference models used provide the sun position (ECI) and the geomagnetic field (NED). The onboard sensors provide the sun vector (BRF), the magnetic-field vector (BRF), the angular velocity (BRF), position, and the velocity (ECEF); and they are modeled for software implementation in this study.

*a. Sun Vector in the Body Frame and Inertial Frame.* Sun sensors on board the CubeSat provide either one-axis or two-axis information in the BRF. We introduce here a sun-sensor model using two-axis information,  $\alpha$  and  $\beta$ , as the true angles measured from the sun sensor. The orientation of the sun sensor in BRF affects the sun vector calculation. To illustrate this procedure, we take the sun sensor mounted on the surface of a positive  $Z$  axis as an example, where  $\alpha$  and  $\beta$  represent the sun angle relative to  $X$  and  $Y$  axes, respectively:

$$\begin{aligned} \tilde{\mathbf{y}}_S^{b,\text{true}} &= \begin{bmatrix} \tan \alpha \\ \tan \beta \\ 1 \end{bmatrix}, & \mathbf{y}_S^{b,\text{true}} &= \frac{\tilde{\mathbf{y}}_S^{b,\text{true}}}{\|\tilde{\mathbf{y}}_S^{b,\text{true}}\|}, \\ \tilde{\mathbf{y}}_S^b &= \begin{bmatrix} \tan(\alpha + \nu_{S,\alpha}) \\ \tan(\beta + \nu_{S,\beta}) \\ 1 \end{bmatrix}, & \mathbf{y}_S^b &= \frac{\tilde{\mathbf{y}}_S^b}{\|\tilde{\mathbf{y}}_S^b\|} \end{aligned} \quad (30)$$

where  $\nu_{S,i}$  is a scalar Gaussian noise with zero mean.

The reference model for the position of the sun in the ECI frame is derived from [30], which sets 1/1/2000 as the reference date for the sun position. The mean longitude of the sun  $L$ , mean anomaly  $g$ , ecliptic longitude  $\lambda$ , obliquity (axial tilt) of the ecliptic  $\varepsilon$ , and distance of the sun from the Earth  $r_s$  are calculated from the following equations, where all the angles are expressed in degrees and the distances in astronomical units:

$$\begin{aligned} L &= 280.460 \text{ deg} + 0.9856474 \text{ deg } JD_{2000} \\ g &= 357.528 \text{ deg} + 0.9856003 \text{ deg } JD_{2000} \\ \lambda &= L + 1.915 \text{ deg } \sin(g) + 0.020 \text{ deg } \sin(2g) \\ \varepsilon &= 23.439 \text{ deg} - 0.0000004 \text{ deg } JD_{2000} \\ r_s &= 1.00014 - 0.01671 \cos(g) - 0.00014 \cos(2g) \end{aligned} \quad (31)$$

Then, the position of the sun in the ECI frame is given by

$$\mathbf{y}_{S,x}^i = r_s \cos(\lambda) \quad \mathbf{y}_{S,y}^i = r_s \cos(\varepsilon) \sin(\lambda) \quad \mathbf{y}_{S,z}^i = r_s \sin(\varepsilon) \cos(\lambda) \quad (32)$$

The application of the  $q$  method is expressed as

$$\mathbf{y}_S^b = \mathbf{A}^{bi} \mathbf{y}_S^i + \boldsymbol{\nu}_S \quad (33)$$

To generate simulated sun-sensor data, we first find the sun vector  $\mathbf{y}_S^i$  in the ECI frame by Eq. (32), which is then converted to the sun vector  $\mathbf{y}_S^b$  in the BRF using Eq. (33). The simulated data are then obtained by reversing the calculation:

$$\alpha = \arccos(\mathbf{y}_{S,1}^{b,\text{true}}) + \nu_{S,\alpha} \quad \beta = \arccos(\mathbf{y}_{S,2}^{b,\text{true}}) + \nu_{S,\beta} \quad (34)$$

*b. Magnetic-Field Vector in the Body Frame and Inertial Frame.* The body-frame magnetic-field vector is provided by the onboard magnetometer as

$$\mathbf{y}_M^b = \mathbf{y}_M^{b,\text{true}} + \boldsymbol{\nu}_M \quad (35)$$

The inertial-frame (ECI) magnetic-field vector is derived from the IGRF-11 model [31], which provides the  $\mathbf{B}$  field in the NED frame. The governing equation for the magnetic induction in the IGRF model is

$$\mathbf{B}(r, \theta, \varphi, t) = -\nabla V \quad (36)$$

where  $V$  is a finite series having the numerical Gauss coefficients  $g_n^m(t)$  and  $h_n^m(t)$  (in nanotesla):

$$\begin{aligned} V(r, \theta, \varphi, t) &= a \sum_{n=1}^N \sum_{m=0}^n \left(\frac{a}{r}\right)^{n+1} [g_n^m(t) \cos(m\varphi) \\ &+ h_n^m(t) \sin(m\varphi)] P_n^m[\cos(90 \text{ deg} - \theta)] \end{aligned} \quad (37)$$

In the preceding expression,  $r$  is the radial distance from the center of the Earth (in kilometers),  $a = 6371.2$  km is the magnetic reference spherical radius,  $\theta$  is the geocentric latitude (in degrees), and  $\varphi$  is the east longitude.  $P_n^m(\cos \theta)$  are the Schmidt seminormalized associated Legendre functions of degree  $n$  and order  $m$ . The Gauss coefficients  $g_n^m(t)$  and  $h_n^m(t)$  are provided for the main field at epochs separated by five-year intervals between 1900 and 2010. The coefficients at a specific time can be found using linear interpolation:

$$\begin{aligned} g_n^m(t) &= g_n^m(T_0) + \dot{g}_n^m(T_0)(t - T_0) \\ h_n^m(t) &= h_n^m(T_0) + \dot{h}_n^m(T_0)(t - T_0) \end{aligned} \quad (38)$$

The Schmidt quasi-normalization function  $P_n^m(\cos \theta)$  is provided in [32] as

$$P_n^m(\mu) = \sqrt{2 \frac{(n-m)!}{(n+m)!}} (1 - \mu^2)^{m/2} \left(\frac{d}{d\mu}\right)^m P_n(\mu) \quad (39)$$

The components of the geomagnetic field in the northward, eastward, and radially inward directions are obtained with the following equations [31]:

$$\begin{aligned} y_{M,x}^n &= \frac{1}{r} \frac{\partial V}{\partial \theta} = \sum_{n=1}^N \sum_{m=0}^n \left(\frac{a}{r}\right)^{n+2} [g_n^m(t) \cos(m\varphi) \\ &+ h_n^m(t) \sin(m\varphi)] P_n^m(\sin(90 \text{ deg} - \theta)) \\ y_{M,y}^n &= \frac{1}{r \sin(90 \text{ deg} - \theta)} \frac{\partial V}{\partial \varphi} \\ &= -\frac{1}{\sin(90 \text{ deg} - \theta)} \sum_{n=1}^N \sum_{m=0}^n \left(\frac{a}{r}\right)^{n+2} m [h_n^m(t) \cos(m\varphi) \\ &- g_n^m(t) \sin(m\varphi)] P_n^m(\cos(90 \text{ deg} - \theta)) \\ y_{M,z}^n &= \frac{\partial V}{\partial r} = \sum_{n=1}^N \sum_{m=0}^n (n+1) \left(\frac{a}{r}\right)^{n+2} [g_n^m(t) \cos(m\varphi) \\ &+ h_n^m(t) \sin(m\varphi)] P_n^m(\cos(90 \text{ deg} - \theta)) \end{aligned} \quad (40)$$

The magnetic-field vector in the ECI frame is obtained using the satellite's position in ECEF (longitude  $\varphi$ , and latitude  $\theta$ ) and  $\mathbf{y}_M^n$ , and an intermediate transformation matrix from ECEF to ECI of  $\mathbf{A}^{ei}$

$$\mathbf{y}_M^i = \mathbf{A}^{ei} \begin{bmatrix} \cos \varphi & -\sin \varphi & 0 \\ \sin \varphi & \cos \varphi & 0 \\ 0 & 0 & 1 \end{bmatrix} \begin{bmatrix} -\sin \theta & 0 & \cos \theta \\ 0 & 1 & 0 \\ -\cos \theta & 0 & \sin \theta \end{bmatrix} \mathbf{y}_M^n \quad (41)$$

To generate simulated magnetometer data in the BRF, we use Eq. (41) to obtain the magnetic-field vector in the ECI frame, which is then converted into the BRF using



$$\mathbf{y}_M^b = \mathbf{A}^{bi} \mathbf{y}_M^i + \mathbf{v}_M \quad (42)$$

where  $\mathbf{v}_M$  is a randomly generated  $3 \times 1$  noise vector with a Gaussian distribution and zero mean. The observations in Eqs. (33) and (42) provide the measurements for the  $q$  method, i.e., with,  $n = 2$  the two body-frame measurements  $\{\mathbf{y}_M^b, \mathbf{y}_S^b\}$  and the two inertial-frame measurements  $\{\mathbf{y}_M^i, \mathbf{y}_S^i\}$  are used in Eqs. (26–29) to obtain the estimate of the quaternion  $\mathbf{y}_q(t)$  using the aforementioned static attitude determination method.

### C. Attitude Estimation with Extended Kalman Filtering

The next step is to find the best estimate of the true system using the dynamic model and measurements. The EKF provides the attitude estimates  $\hat{\boldsymbol{\omega}}(t)$  and the quaternion estimate  $\hat{\mathbf{q}}(t)$  using the (static) estimate of the quaternion  $\mathbf{y}_q(t)$ , the gyroscope measurements denoted by  $\mathbf{y}_G^b(t)$ , and the dynamic equations [Eqs. (20) and (21)].

Rate gyroscopes provide the CubeSat's angular velocity in the BRF. The gyroscope measurements  $\mathbf{y}_G^b(t)$  are given by

$$\mathbf{y}_G^b(t) = \boldsymbol{\omega}(t) + \mathbf{v}_G(t) \quad (43)$$

where  $\boldsymbol{\omega}(t)$  is the true angular velocity, and  $\mathbf{v}_G(t)$  is the white noise ( $3 \times 1$ ) vector. To obtain simulated gyroscope data, we use Eq. (43), where  $\boldsymbol{\omega}(t)$  is from Eq. (20) and  $\mathbf{v}_G(t)$  is a randomly generated  $3 \times 1$  noise vector with Gaussian distribution and zero mean.

To implement the EKF, we rewrite Eqs. (20) and (21) in state-space form as

$$\begin{aligned} \dot{\mathbf{x}}(t) &= \begin{pmatrix} \dot{\boldsymbol{\omega}} \\ \dot{\mathbf{q}} \end{pmatrix} = \begin{pmatrix} \mathbf{I}^{-1} \mathbf{T}_C - \mathbf{I}^{-1} (\boldsymbol{\omega} \times \mathbf{I} \boldsymbol{\omega}) \\ \frac{1}{2} \boldsymbol{\Omega}(\boldsymbol{\omega}) \mathbf{q} \end{pmatrix} + \mathbf{w}(t) \\ \mathbf{y}(t) &= \begin{pmatrix} \boldsymbol{\omega} \\ \mathbf{q} \end{pmatrix} + \mathbf{v}(t) = \begin{pmatrix} \mathbf{y}_G \\ \mathbf{y}_q \end{pmatrix} \end{aligned} \quad (44)$$

where  $\mathbf{w}(t)$  is a Gaussian process noise with covariance matrix  $\mathbf{Q}$  and zero mean, and  $\mathbf{v}(t)$  is the Gaussian observation (sensor) noise with covariance matrix  $\mathbf{R}$  and zero mean. The covariance matrix  $\mathbf{R}$  is a square diagonal matrix with  $\sigma$  corresponding to the gyroscope represented by the first three entries and the  $\sigma$  of the sun sensors represented by the last four entries. The covariance matrix  $\mathbf{Q}$  has to be tuned in order to achieve good EKF performance. Using the notation  $G_k = G(k\Delta t)$  to denote the discrete-time representation of a quantity  $G(t)$ , the discrete-time state-space representation of Eq. (44) is

$$\mathbf{x}_k = \mathbf{f}(\mathbf{x}_{k-1}, \mathbf{u}_{k-1}) + \mathbf{w}_{k-1} \quad \mathbf{y}_k = \mathbf{h}(\mathbf{x}_k) + \mathbf{v}_k \quad (45)$$

where

$$\mathbf{x}_k = \begin{bmatrix} \boldsymbol{\omega}_k \\ \mathbf{q}_k \end{bmatrix}$$

is the process state (plant);  $\mathbf{u}_k$  is the control input (e.g.,  $\mathbf{T}_C$

$$\mathbf{f}(\mathbf{x}_{k-1}, \mathbf{u}_{k-1}) = \begin{bmatrix} \boldsymbol{\omega}_{k-1} \\ \mathbf{q}_{k-1} \end{bmatrix} + \Delta t \begin{bmatrix} \mathbf{I}^{-1} [\mathbf{T}_C + \mathbf{T}_D - (\boldsymbol{\omega}_{k-1} \times \mathbf{I} \boldsymbol{\omega}_{k-1})] \\ \frac{1}{2} \boldsymbol{\Omega}(\boldsymbol{\omega}_{k-1}) \mathbf{q}_{k-1} \end{bmatrix} \quad (46)$$

and

$$\mathbf{y}_k = \begin{bmatrix} \mathbf{y}_{G,k} \\ \mathbf{y}_{q,k} \end{bmatrix}$$

with  $\mathbf{y}_{G,k}$  given in Eq. (43) and  $\mathbf{y}_{q,k}$  given by Eq. (29). Due to the nonlinearity of Eq. (46), we first linearize it and obtain the Jacobian matrices  $\mathbf{F}$  and  $\mathbf{H}$ :

$$\mathbf{F}_{k-1} = \left. \frac{\partial \mathbf{f}}{\partial \mathbf{x}} \right|_{\hat{\mathbf{x}}_{k-1}^+, \mathbf{u}_{k-1}} \quad \mathbf{H}_k = \left. \frac{\partial \mathbf{h}}{\partial \mathbf{x}} \right|_{\hat{\mathbf{x}}_{k-1}} = \mathbf{I}_{7 \times 7} \quad (47)$$

where the superscripts  $-$  and  $+$  represent a priori and a posteriori state estimates, and EKF is implemented as a two-step process. In the predictor step,

$$\hat{\mathbf{x}}_k^- = \mathbf{f}(\hat{\mathbf{x}}_{k-1}, \mathbf{u}_{k-1}) \quad \mathbf{P}_k^- = \mathbf{F}_{k-1} \mathbf{P}_{k-1} \mathbf{F}_{k-1}^T + \mathbf{Q}_{k-1} \quad (48)$$

where  $\mathbf{P}$  is the error covariance matrix. In the update step, the Kalman filter gain is calculated first:

$$\mathbf{K}_k = \mathbf{P}_k^- \mathbf{H}_k^T (\mathbf{H}_k \mathbf{P}_k^- \mathbf{H}_k^T + \mathbf{R}_k)^{-1} \quad (49)$$

and the state estimate is updated with the optimal gain:

$$\hat{\mathbf{x}}_k^+ = \hat{\mathbf{x}}_k^- + \mathbf{K}_k [\mathbf{y}_k - \mathbf{h}(\hat{\mathbf{x}}_k^-)] \quad (50)$$

The error covariance matrix is updated for use at the predictor step:

$$\mathbf{P}_k^+ = [\mathbf{I}_{7 \times 7} - \mathbf{K}_k \mathbf{H}_k] \mathbf{P}_k^- = [\mathbf{I}_{7 \times 7} - \mathbf{K}_k] \mathbf{P}_k^- \quad (51)$$

### D. Attitude Control

In this section, we first introduce the thruster model and control implementation, and we discuss the change of angular velocity during one set of thruster firings, as well as the thruster arrangement. Then, we introduce the attitude control method using  $\mu$ PPTs. Reference [22] discussed the pulsewidth pulse-frequency modulation method; however, due to the fixed pulse duration and the restricted pulse frequency  $f_P$  of the  $\mu$ PPTs, we propose a two-step process for attitude control. As shown in Fig. 12, the process commences with the attitude determination and estimation to produce the estimates  $\hat{\boldsymbol{\omega}}(t)$  and  $\hat{\mathbf{q}}(t)$ . Then, the estimated states  $\hat{\boldsymbol{\omega}}(t)$  and  $\hat{\mathbf{q}}(t)$  from the EKF are used in the proportional and derivative control algorithm in place of  $\boldsymbol{\omega}(t)$  and  $\mathbf{q}(t)$  in order to calculate the desired torque  $\mathbf{T}_{des}$ . Note that the actuator system cannot realize the desired torque  $\mathbf{T}_{des}$  using the  $\mu$ PPTs due to the fixed impulse bit; as a consequence, a thruster-allocation method is used to determine the optimal thruster-firing combination  $\mathbf{z} \in R^n$  such that the angle between  $\mathbf{T}_{des}$  [the designed control input using Eqs. (20) and (21)] and control output  $\mathbf{T}_C$  [the actual input to Eqs. (20) and (21), which is the output of the  $\mu$ PPTs] is minimal. Finally, we compute the control torque output  $\mathbf{T}_C$  and use it to actuate the control system given by Eqs. (20) and (21). One advantage of using the proposed two-step process for attitude control (i.e., a separate control algorithm and thruster allocation) is to increase the robustness of attitude control in the event of a thruster failure.

#### 1. Thruster Model and Control Implementation

The thruster model is derived in the BRF as shown in Fig. 1a. The origin is placed in the center of mass of the CubeSat and the Z axis is along the long axis, and it is positive toward the thruster side. Thrusters numbered 1 to 4 are on the top layer and 5 through 8 are on the second layer, as shown in Fig. 13. The positioning of the thrusters provides redundancy in attitude control. The  $\mu$ PPT operates as shown in Fig. 6.

A discrete-time dynamic model of Eq. (20) is required due to the pulsed operation of the thrusters:

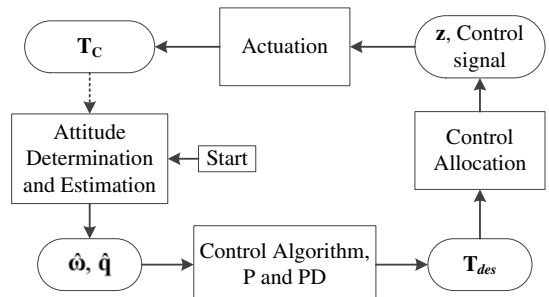


Fig. 12 Flowchart for attitude control.

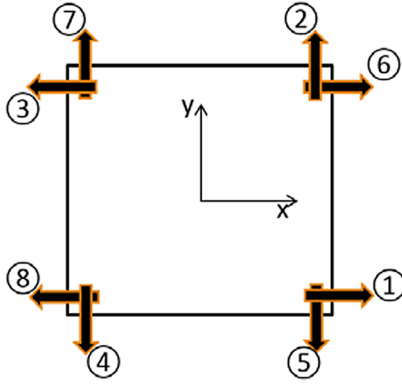


Fig. 13 Top view of thruster arrangement (1, 2, 3, and 4 are on the top layer).

$$I \frac{\Delta \omega}{\Delta t} = [T_C + T_D - (\omega \times I \omega)] \quad (52)$$

The torque  $T_i$ , produced by a single firing of one  $\mu$ PPTs during  $\tau_p$ , is

$$T_i = F(\mathbf{r}_{\text{eff},i} \times \mathbf{n}_i) = \frac{I_{\text{bit}}}{\tau_p} (\mathbf{r}_{\text{eff},i} \times \mathbf{n}_i) \quad (53)$$

and therefore, the control torque  $T_C$  produced by a set of active thrusters during  $\tau_p$  is

$$T_C = \sum_{i \in I(t)} \left[ \frac{I_{\text{bit}}}{\tau_p} (\mathbf{r}_{\text{eff},i} \times \mathbf{n}_i) \right] \quad (54)$$

where  $I(t) = \{1, 2, \dots\}$  is the set of active thrusters at time  $t$  that will be determined in the thruster-allocation section. The effective position vector of the thrusters from the center of mass is defined as

$$\mathbf{r}_{\text{eff},i} = \mathbf{r}_i - \mathbf{r}_{\text{com}} \quad (55)$$

where  $\mathbf{r}_i$  is the position vector of the thruster relative to the CubeSat's geometrical center, and  $\mathbf{r}_{\text{com}}$  is the vector from the geometric center to the center of mass. Assuming that the control torque is applied over a time period  $\Delta t = \tau_p$ , substitution of Eq. (54) into Eq. (52) results in

$$I \Delta \omega = \sum_{i \in I(t)} [I_{\text{bit}} (\mathbf{r}_{\text{eff},i} \times \mathbf{n}_i)] + T_D \tau_p - (\omega \times I \omega) \tau_p \quad (56)$$

Scaling of the preceding equation can be obtained using typical values for  $I_x = 0.03 \text{ kg} \cdot \text{m}^2$ ,  $I_{\text{bit}} = 40 \times 10^{-6} \text{ N} \cdot \text{s}$ ,  $\|\mathbf{r}_{\text{eff},i}\| = 0.15 \text{ m}$ ,  $\|\mathbf{T}_D\| = 6 \times 10^{-6} \text{ N} \cdot \text{m}$ ,  $\tau_p \sim 10^{-6} \text{ s}$ , and  $\omega < 0.15 \text{ rad/s}$ . The last two terms in the right-hand side of Eq. (56) can be neglected, and we obtain

$$\Delta \omega = I^{-1} \sum_{i \in I(t)} [I_{\text{bit}} (\mathbf{r}_{\text{eff},i} \times \mathbf{n}_i)] \quad (57)$$

Notice that the pulse frequency  $f_p$  does not affect the change in angular velocity for each firing but, given a time span, the frequency will affect the total number of firings, which in turn will influence the total change of angular velocity.

We also account for the shot-to-shot variation, so the output  $I_{\text{bit}}$  is equal to the designed  $\overline{I_{\text{bit}}}$  plus a random error with a Gaussian distribution and standard deviation of 1%:

$$I_{\text{bit}} = \overline{I_{\text{bit}}} + \delta(t) \quad (58)$$

We introduce a fixed error for the thrust vector  $\mathbf{n}_i$  to account for thrust misalignment with respect to the BRF. The thrust vector  $\mathbf{n}_i$  will be rotated by 0.5 deg in each of the two offaxis directions to simulate a constant error introduced during structure integration.

## 2. Attitude Control Using Proportional and Derivative Controller, as Well as Thruster Allocation

a. *Stabilization.* During the stabilization phase, we do not require attitude determination but only the estimate of the angular rate  $\hat{\omega}$ . The desired torque is given by the proportional controller

$$\mathbf{T}_{\text{des}} = -\mathbf{K}(\hat{\omega} - \omega_{\text{des}}) \quad (59)$$

where  $\mathbf{K}$  is a user-defined proportional gain matrix, and  $\omega_{\text{des}}$  is the desired angular velocity. If the actuator has no dynamics, then this  $\mathbf{T}_{\text{des}}$  would be implemented in Eq. (20) as  $\mathbf{T}_C$ . However, as mentioned previously, we introduce the thruster-allocation method to find the best thruster-firing combination that minimizes the angle between the desired torque  $\mathbf{T}_{\text{des}}$  and the control torque  $\mathbf{T}_C$  delivered by the active  $\mu$ PPTs.

b. *Target Pointing (Slewing) and Spinning.* A general proportional-derivative (PD) controller using Euler error angles  $\boldsymbol{\varphi}$  is used as the control architecture:

$$\mathbf{T}_{\text{des}} = -\mathbf{K}_P \boldsymbol{\varphi} - \mathbf{K}_d(\hat{\omega} - \omega_{\text{des}}) \quad (60)$$

In the case of sun pointing, two of the Euler angles can be obtained directly from the sun sensors. In general, they are given by

$$\boldsymbol{\varphi} = \begin{bmatrix} \tan^{-1}(2\tilde{q}_1\tilde{q}_4 + 2\tilde{q}_2\tilde{q}_3, 1 - 2\tilde{q}_1^2 - 2\tilde{q}_2^2) \\ \sin^{-1}(2\tilde{q}_4\tilde{q}_2 - 2\tilde{q}_3\tilde{q}_1) \\ \tan^{-1}(2\tilde{q}_3\tilde{q}_4 + 2\tilde{q}_1\tilde{q}_2, 1 - 2\tilde{q}_2^2 - 2\tilde{q}_3^2) \end{bmatrix} \quad (61)$$

where the function,  $\tan^{-1}$ , with two arguments is the four-quadrant inverse tangent, which differs from the regular inverse tangent by having an expanded output range from  $[-\pi/2, \pi/2]$  to  $[-\pi, \pi]$ . The error quaternion  $\tilde{q}$  is defined in [16] as

$$\tilde{q} = \begin{bmatrix} \tilde{q}_1 \\ \tilde{q}_2 \\ \tilde{q}_3 \\ \tilde{q}_4 \end{bmatrix} = \begin{bmatrix} q_{\text{des},4} & q_{\text{des},3} & -q_{\text{des},2} & -q_{\text{des},1} \\ -q_{\text{des},3} & q_{\text{des},4} & q_{\text{des},1} & -q_{\text{des},2} \\ q_{\text{des},2} & q_{\text{des},1} & q_{\text{des},4} & -q_{\text{des},3} \\ q_{\text{des},1} & q_{\text{des},2} & q_{\text{des},3} & q_{\text{des},4} \end{bmatrix} \begin{bmatrix} q_1 \\ q_2 \\ q_3 \\ q_4 \end{bmatrix} \quad (62)$$

where  $q_{\text{des}}$  can be found in the reference model. In Eq. (60),  $\mathbf{K}_P$  and  $\mathbf{K}_d$  are proportional and derivative gain matrices, which are determined by the moment of inertia of the spacecraft:

$$\mathbf{K}_p = 2\omega_n^2 \mathbf{I}, \quad \mathbf{K}_d = 2\zeta\omega_n \mathbf{I} \quad (63)$$

where  $\omega_n$  and  $\zeta$  are the natural frequency and damping ratio, which require tuning in order to achieve acceptable attitude control performance. Due to the limited control authority of a pulsed thruster, the damping ratio does not work in the same way as with a traditional controller. In this case, the direction of the desired torque provided by the PD control scheme is more important than the magnitude of the torque. Different gain matrices may be chosen based on different specifications and arrangement of the  $\mu$ PPT. The performance of the controller also depends on the accuracy of the sensor [i.e., the statistics of the noise  $\mathbf{v}(t)$  in Eq. (44) and the magnitude of the environmental disturbances  $\mathbf{T}_D(t)$  in Eq. (20)].

c. *Optimal Controller Allocation.* The angle between the torque output  $\mathbf{T}_C$  and the desired torque  $\mathbf{T}_{\text{des}}$  (i.e., the cost function) must be minimized in order to obtain the best approximation of  $\mathbf{T}_{\text{des}}$ . This is solved with a nonlinear binary optimization:

$$\begin{aligned} \min_z & \left\| \cos^{-1} \left( \frac{\mathbf{B}\mathbf{z} \cdot \mathbf{T}_{\text{des}}}{\|\mathbf{B}\mathbf{z}\| \|\mathbf{T}_{\text{des}}\|} \right) \right\| \\ \text{subject to: } & \mathbf{z} \in \{0, 1\}^n \quad \text{and} \quad \sum_{i=1}^n z_i \leq 5 \end{aligned} \quad (64)$$

where  $\mathbf{z}$  is a  $n \times 1$  vector indicating the status of all thrusters where each entry has value of either zero (off) or one (on); and  $\mathbf{B} \in \mathbf{R}^{m \times n}$  is

the control effectiveness matrix (i.e.,  $\mathbf{B}_i = (\mathbf{r}_{\text{eff},i} \times \mathbf{n}_i)$ ), where  $n = 8$  is the dimension of  $\mathbf{z}$  and  $m = 3$  is the dimension of the torque vector  $\mathbf{T}_{\text{des}}$  [33]. Notice that  $\mathbf{z}$  is the control signal that determines which thruster to fire, and  $\mathbf{B}\mathbf{z}$  is the actuator output (also equal to  $\mathbf{T}_C$ ). The second condition in Eq. (64) is the constraint from the thruster electronics. Preliminary design of the thruster module has constrained the power distribution to an upper limit of five thrusters at one time, meaning that, at any instance, at most, five thrusters can be fired; that is, the cardinality of the set  $\mathbf{I}(t)$  is, at most, five at any instance. The solution to this optimization problem provides the best thruster-firing combinations to accommodate the direction of the desired torque  $\mathbf{T}_{\text{des}}$ .

If the cost function is twice continuously differentiable, the solution to the optimization problem [Eq. (64)] can be obtained by first convexifying the problem and then solving a sequence of subproblems, for which the solutions form a trajectory that leads to the final solution [34]. However, this is not the case, because the cost function cannot be simplified; the only way to solve this optimization problem is by the method of exhaustion. Fortunately, there are only eight binary variables, which require 255 repeated calculations, making it practical to solve on board in real time. The cosine is an even function with  $\cos(0) = 1$ . Therefore, the cost function can be reduced to the simpler form

$$\min_{\mathbf{z}} \left\{ -\frac{\mathbf{B}\mathbf{z} \cdot \mathbf{T}_{\text{des}}}{\|\mathbf{B}\mathbf{z}\| \|\mathbf{T}_{\text{des}}\|} \right\}$$

$$\text{subject to } \mathbf{z} \in \{0, 1\}^n \quad \text{and} \quad \sum_{i=1}^n z_i \leq 5 \quad (65)$$

This reduces the computational cost. Although the improvement is at the level of tens of milliseconds, it can be significant in cases where  $\mathbf{z}$  has a large dimension. When the desired attitude is achieved, we implement a dead-zone modification in order to avoid unnecessary thruster firings:

$$T_{\text{des},i} = \begin{cases} T_{\text{des},i}, & |T_{\text{des},i}| > T_{\text{crit}} \\ 0, & |T_{\text{des},i}| \leq T_{\text{crit}} \end{cases} \quad (66)$$

where  $T_{\text{crit}}$  is the critical torque threshold, which is determined based on the moment of inertia  $\mathbf{I}$ , the effectiveness matrix  $\mathbf{B}$ , and the impulse bit  $I_{\text{bit}}$ . When the desired torque is below the critical torque level, no thruster will be fired, which means that, if  $T_{\text{des}} = 0$ , then  $\mathbf{z}$  is a  $8 \times 1$  vector of zeros and  $\mathbf{I}(t)$  is the null set.

This control algorithm is processed no more frequently than the pulse frequency of the  $\mu\text{PPT}$ . Therefore, for a  $\mu\text{PPT}$  with  $f_p = 1$  Hz, the algorithm will be evaluated, at most, once every second. The advantage of using this method is that, in the event of thruster failure, simply changing the  $\mathbf{B}$  matrix in the optimization will suffice.

## V. Simulation Results

### A. Input Parameters

For simulation purposes, we use MATLAB® [35] to implement the attitude control for the CubeSat shown in Fig. 1b. The center of mass of the CubeSat in the BRF is located at  $[0.5 \ 1.5 \ -1]$  cm relative to the geometric center. The inertia matrix (nondiagonal) for the CubeSat shown in Fig. 1b is estimated as

$$\mathbf{I} = \begin{bmatrix} 0.03 & 0.0005 & 0.0005 \\ 0.0005 & 0.03 & 0.0005 \\ 0.0005 & 0.0005 & 0.006 \end{bmatrix} \text{ kg} \cdot \text{m}^2$$

We assume that the  $\mu\text{PPT}$  has  $I_{\text{bit}} = 40 \mu\text{N} \cdot \text{s}$  with a random error of normal 1% and a pulse frequency of  $f_p = 1$  Hz. The thrust vector has a fixed error of 1% to simulate the error introduced in the thruster-structure integration. Since the orbit propagation was not considered in this study, the orbital parameters of the CubeSat are not evaluated. To study the feasibility of a  $\mu\text{PPT}$  in providing the desired attitude

control, we introduce both periodic and constant disturbances based on the maximum disturbances encountered in the orbit. These disturbances are applied to all three axes.

Typical sensor errors are introduced in the simulation. Sun sensors are assumed with an error of  $0.2 \text{ deg}$  ( $3\sigma$ ), the gyroscope is assumed with an error of  $0.05 \text{ deg/s}$ , and the magnetometer is assumed with an error of  $250 \text{ nT}$ . To simulate the realistic situation, EKF [36] is implemented for measurement filtering.

### B. Detumbling Scenario

After being deployed from the launch vehicle, a CubeSat usually has random rotations, and the first phase of attitude control is to stabilize. The initial body rotation is typically  $5 \text{ deg/s}$ , and we assume that each axis has a rotation of  $5 \text{ deg/s}$ . After stabilization, the CubeSat should have a minimum angular rotation as some onboard devices are powered on.

As shown in Fig. 14, the rotational kinetic energy decreases almost linearly. The thruster has a fixed impulse bit, so the result is different from the usual controller where an exponential decay is expected. From the data presented in Figs. 7 and 8, in Sec. III.B, we find that a set of six thrusters, operating with an impulse bit and pulse frequency of  $40 \mu\text{N} \cdot \text{s}$  and  $1 \text{ Hz}$ , respectively, is capable of completing maneuvers with an angular momentum rate of under  $5 \mu\text{N} \cdot \text{s/s}$ . So, for a stabilization of  $\Delta\omega = 5 \text{ deg/s}$ , the time estimate is shown in Fig. 15 to be less than 10 min, which is consistent with the result presented here. The stabilization time is expected to be less than an estimate based solely on the rate, due to the addition of two thrusters.

Figure 16 shows the firing sequence of  $\mu\text{PPT}$ s for the 3U CubeSat during detumbling and compensation of periodic disturbances. The areas filled with lines in Fig. 16 indicate that the specific thruster is on full operation. After the CubeSat is stabilized within 8 min, there are scattered firings as shown in Fig. 16. The scattered firings after 8 min compensate for the rotation due to disturbance torques. Comparing this with the result due to a constant disturbance torque in Fig. 17, the thrusters can stabilize the CubeSat in both situations, and the time for initial stabilization is the same; however, it requires more firings to compensate for the constant disturbance torques that act on the spacecraft continuously.

As noted earlier, to compensate for a constant disturbance requires a set of six thrusters with  $40 \mu\text{N} \cdot \text{s}$  with  $1 \text{ Hz}$  frequency. With the specific arrangement of thrusters in this study,  $n = 2$  in Eq. (13) and, as a result, none of the thrusters is overloaded. The  $\mu\text{PPT}$  is adequate to stabilize the CubeSat, even during the worst case of disturbance. To meet the power constraints, a typical shot energy of  $1.5 \text{ J}$  is used to calculate the power consumption of a  $\mu\text{PPT}$  module during detumbling. In Fig. 18, the average power consumption for detumbling is approximately  $6 \text{ W}$  and, after 8 min, when the CubeSat is stabilized, the average power consumption is less than  $1 \text{ W}$  for disturbance

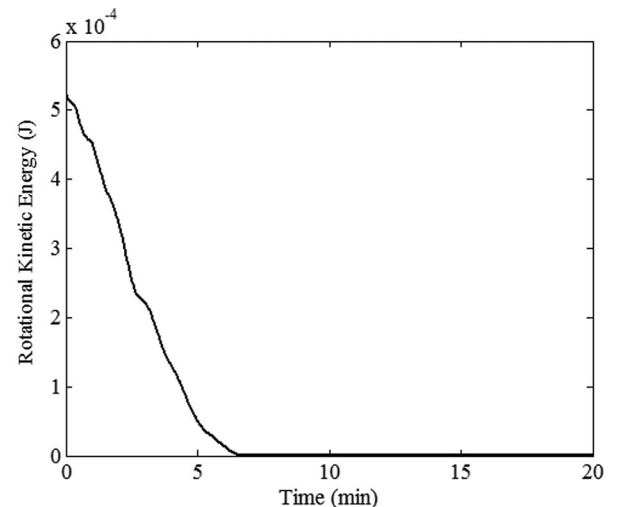
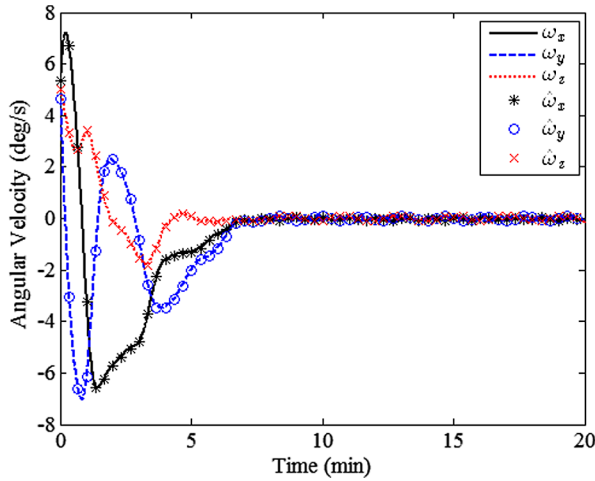


Fig. 14 Rotational kinetic energy of a 3U CubeSat undergoing detumbling with  $\mu\text{PPT}$ s.



**Fig. 15** Angular velocity of a 3U CubeSat undergoing detumbling with  $\mu$ PPTs.

torque compensation. With double-deployed solar panels, shown in Fig. 1b, the total power during sunlight is rated at 20 W; as a result, the power consumption is well within the constraint of a CubeSat power budget. With a total of 1771 firing during the 20 min period, the mass consumption is estimated at about 24 mg.

### C. Pointing Scenario

A CubeSat mission considered in this scenario involves sun observation or target tracking. In this simulation, the initial error angle about the sun is 68 deg, and it is required that the CubeSat be controlled to correctly point toward the sun within 0.5 deg. This leads us to the pointing requirement where the CubeSat needs to be oriented correctly to have the desired field of view over a certain target. The allowable time span for the maneuver is set to 20 min.

The pointing accuracy is limited by the sensor accuracy. A fine sun sensor has accuracy within 0.1 deg; however, a coarse sun sensor, which is more commonly encountered, will have an accuracy of 0.1 to 1 deg. Figure 19 shows the pointing error during the 20 min simulation. The horizontal line at approximately 0.25 deg shows the

radius of the sun in the view from the CubeSat. The pointing accuracy can be achieved under 0.5 deg. In Fig. 20, the angular velocities for the first 2 min depict the fastest slew maneuver that can be achieved by  $\mu$ PPTs. The angular velocity reaches maximum and starts to decrease immediately, implying the idle (or coasting) period is 0%.

In Fig. 21, the average number of pulses per thruster is 472, with a minimum of 419 and a maximum of 517. Assuming that the CubeSat is always in the view of the sun for a desired mission time of one year, then the average number of pulses is approximately 12 million/thruster and the maximum number of pulses is 13 million/thruster. Similar to detumbling, we show in Fig. 22 the power consumption of the  $\mu$ PPT module during pointing maneuvers. It is expected that, at most, five thrusters will fire at the same time and under normal operation; two to four thrusters fire constantly to correct the pointing and compensate for the disturbance torques, so the power consumption is between 3 and 6 W. With a total of 3776 firing during the 20 min period, the mass consumption is estimated at about 51 mg.

### D. Pointing and Spinning Scenario

In this simulation, we evaluate the control strategy for spinning and pointing. The strategy will orient the CubeSat toward the sun within 0.5 deg and then start to spin it to 3 deg/s around the pointing axis. Figures 23 and 24 shows that the CubeSat first enters the pointing phase to obtain the desired attitude. Then, it starts to spin around the pointing axis (X axis in Fig. 1a). As the CubeSat is constantly adjusting the attitude for pointing, thrusters may fire for pointing correction, and no (or fewer) thrusters will be available for spinning.

The time to achieve spinning with pointing is longer than that for just the spinning, as shown in Fig. 25. If the desired spin rate is 3 deg/s from a static state, Fig. 24 shows the time to reach stabilized spinning is less than 8 min (from 4 to 12 min), whereas the time for the spinning-only maneuver to take place is less than 2 min.

### E. Comparison of Thruster-Allocation and Paired-Firing Methods During Failure

In this section, we compare simulation results during pointing maneuvers with the thruster-allocation method presented in this paper and the paired-firing method by Gatsonis et al. [1]. We set thruster 3 to be inoperative for both firing methods and assume detection of the failure. Paired firing will use the same technique, with

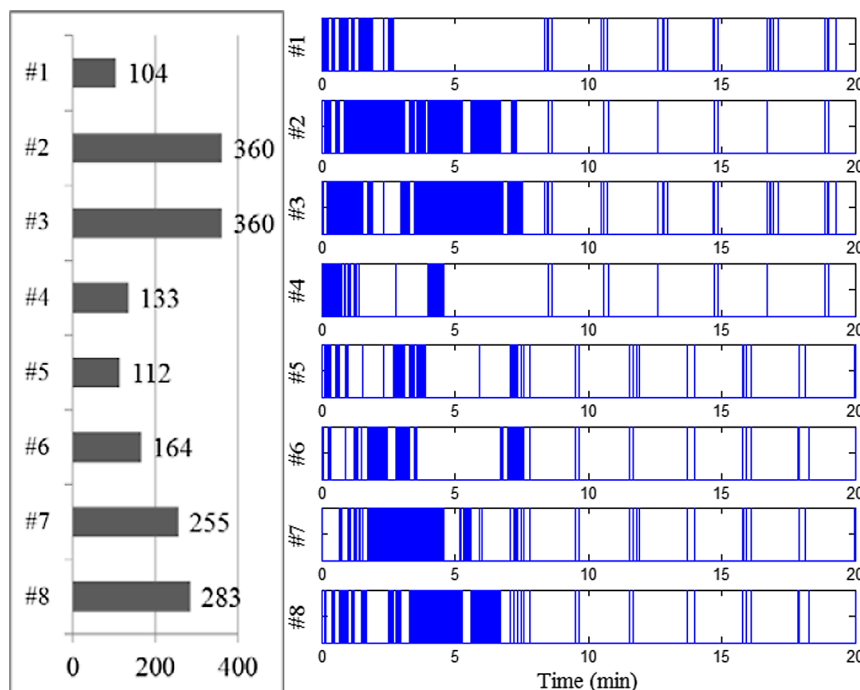


**Fig. 16** Firing sequence of  $\mu$ PPTs on a 3U CubeSat during detumbling and compensation of periodic disturbance: total number of firings from each thruster (left), and time of occurrence for each firing indicated by a line (right).

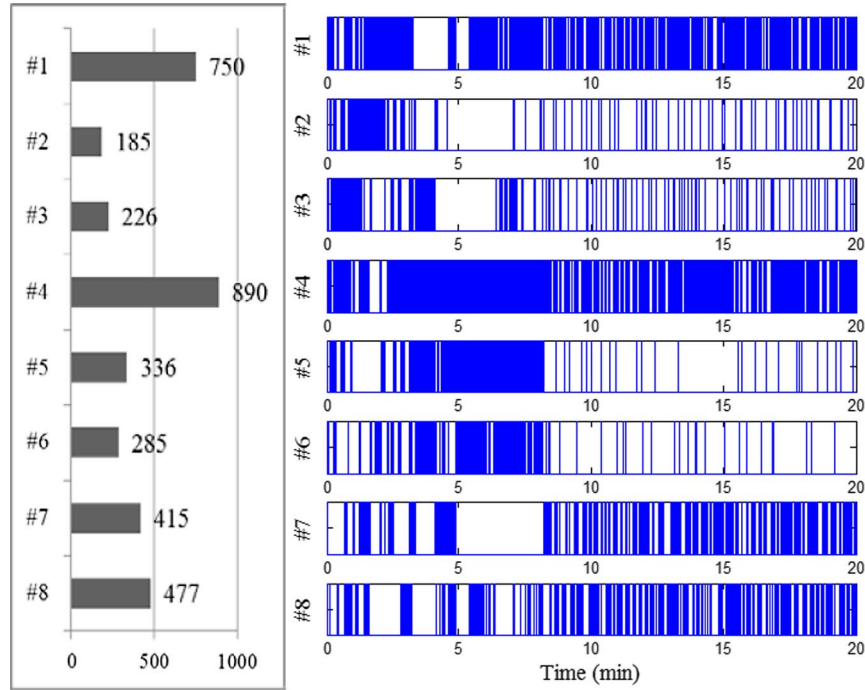


Fig. 17 Firing sequence of  $\mu$ PPTs on a 3U CubeSat during detumbling and compensation of the maximum constant disturbance: total number of firings from each thruster (left), and time of occurrence for each firing indicated by a line (right).

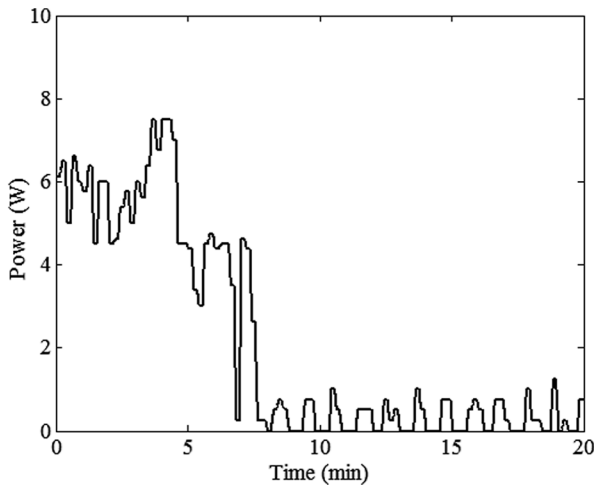


Fig. 18 Power consumption of  $\mu$ PPTs on a 3U CubeSat during detumbling and compensation of periodic disturbance torques.

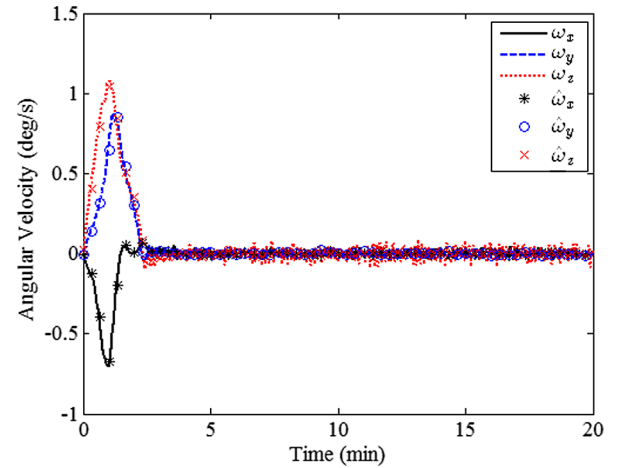


Fig. 20 Angular velocity of a 3U CubeSat undergoing pointing using  $\mu$ PPTs.

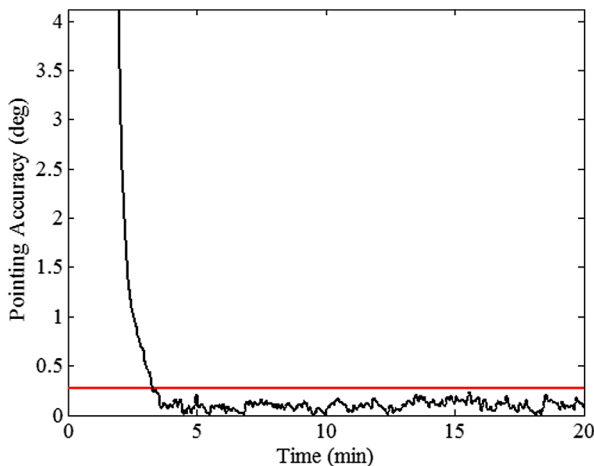


Fig. 19 Pointing angle error of a 3U CubeSat using  $\mu$ PPTs.

the optimal angular velocity threshold being halved due to the loss of half-control authority; but, when the pair of thrusters that includes thruster 3 is commanded to fire, only the operational thruster will fire. With the separate control algorithm and thruster-allocation method, as described in Sec. IV.D.2, the control effectiveness matrix needs to be modified to accommodate the situation, and the gain in the control algorithm will be affected, as was the case when decreasing the threshold for the paired-firing technique.

Figure 26 shows the pointing accuracy and demonstrates that both methods are able to orient the CubeSat properly with the thruster-allocation method being more robust. The time required to achieve pointing and stabilization with thruster failure is slightly longer than that without failure, as a comparison with Fig. 19. A comparison of the angular velocity of the CubeSat in Fig. 27 shows that the paired-firing method does not eliminate the constant angular velocity around the pointing axis because it cannot properly distribute the torque. In contrast, the thruster-allocation method shows that the impact of the thruster failure is minimal.

Without loss of control authority, we next set thrusters 3 and 6 as inoperative. The simulation results are shown in Figs. 28 and 29. Both

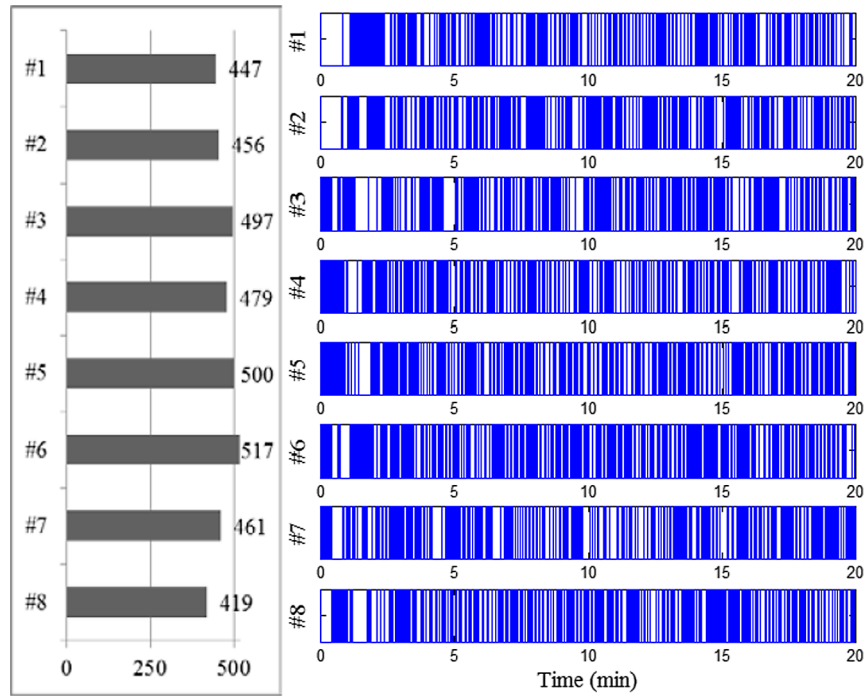


Fig. 21 Firing sequence of  $\mu$ PPTs on a 3U CubeSat during target (sun) pointing: total number of firings from each thruster (left), and time of occurrence for each firing (right). Each line indicates one firing.

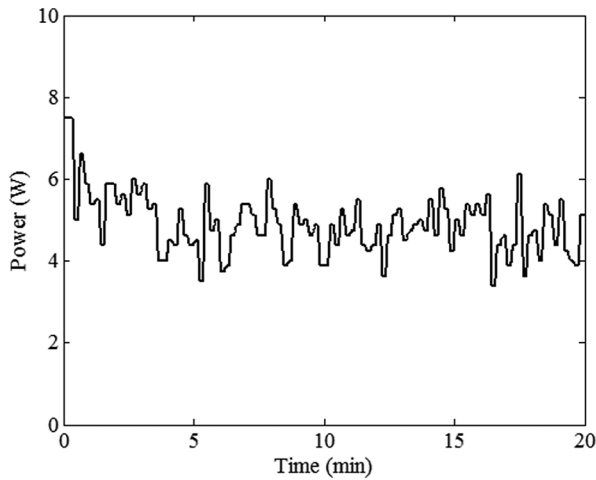


Fig. 22 Power consumption of  $\mu$ PPTs on a 3U CubeSat during pointing maneuver.

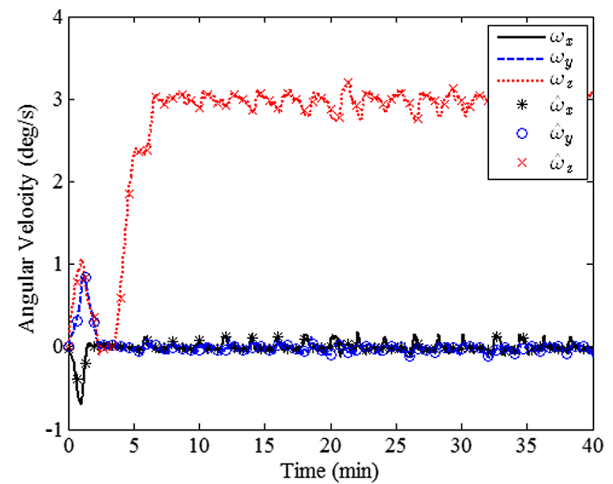


Fig. 24 Angular velocity of a 3U CubeSat undergoing pointing and spinning to 3 deg/s with  $\mu$ PPTs.

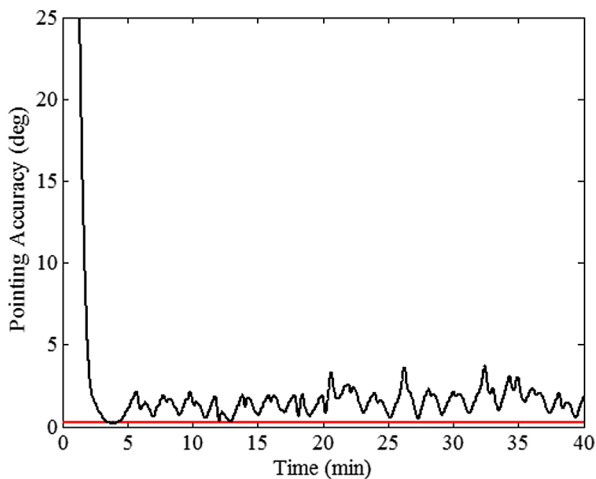


Fig. 23 Pointing angle error of a 3U CubeSat undergoing pointing and spinning maneuvers using  $\mu$ PPTs.

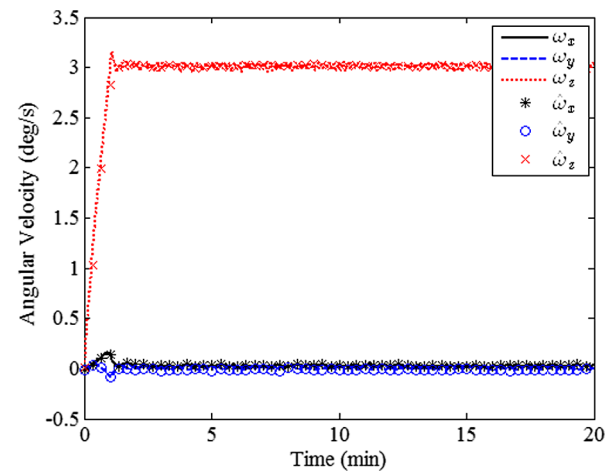


Fig. 25 Angular velocity of a 3U CubeSat undergoing spinning to 3 deg/s with  $\mu$ PPTs without pointing.

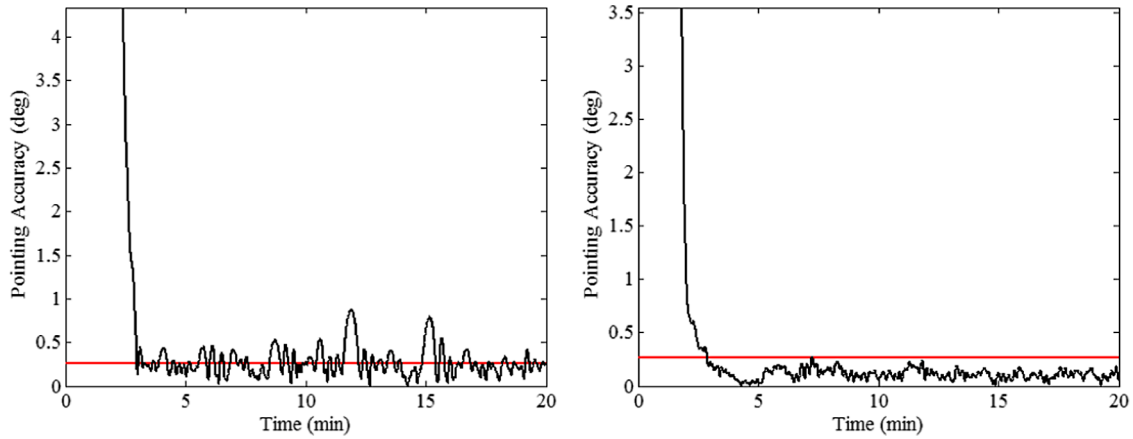


Fig. 26 Pointing angle error of a 3U CubeSat using  $\mu$ PPTs with paired firing (left) and thruster allocation (right) under thruster failure.

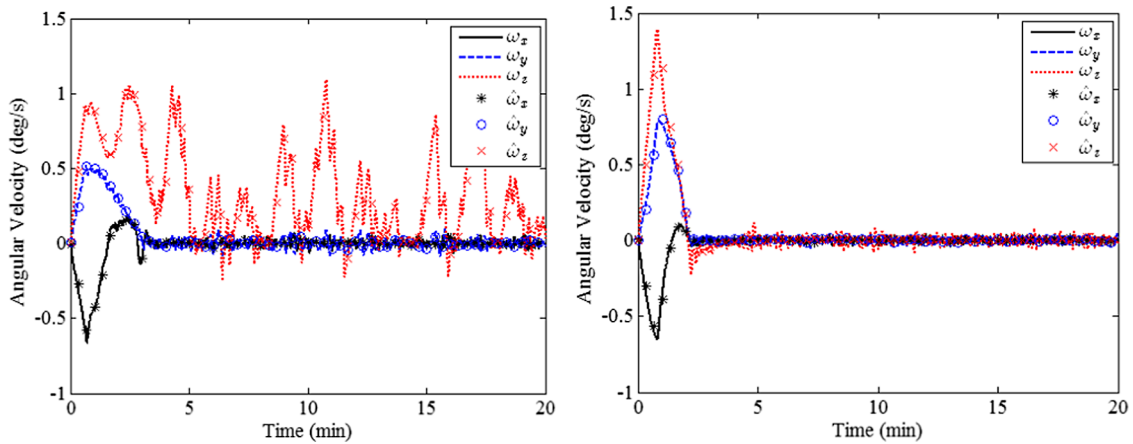


Fig. 27 Angular velocity of a 3U CubeSat using  $\mu$ PPTs with paired firing (left) and thruster allocation (right) assuming a single thruster failure.

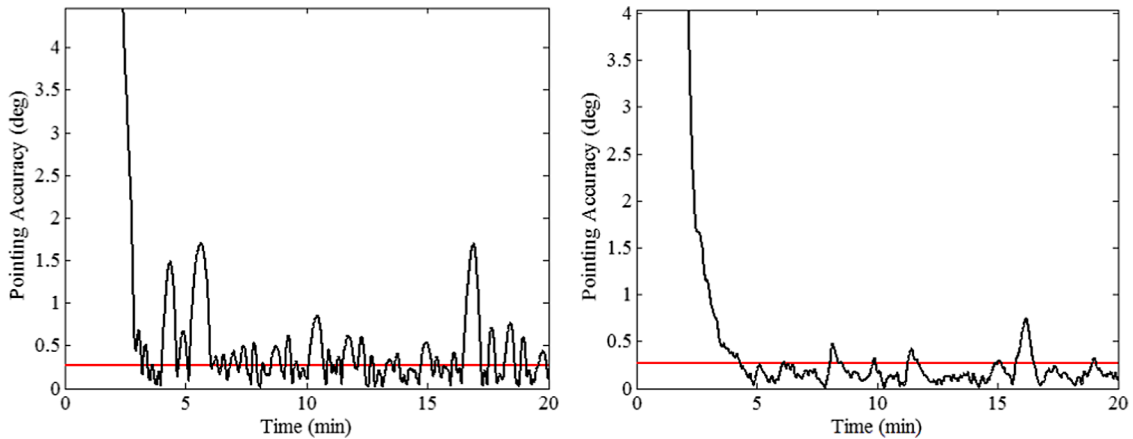


Fig. 28 Pointing angle error of a 3U CubeSat using  $\mu$ PPTs with paired firing (left) and thruster allocation (right) assuming two failed thrusters.

control methods achieve pointing, with the thruster-allocation method exhibiting better performance. As before, the paired-firing method fails to stabilize the rotation along the Z axis.

Finally, we assume that thrusters 3, 6, and 7 are inoperative, with simulation results for the pointing maneuver shown in Figs. 30 and 31. The paired-firing method is not able to control the attitude properly and cannot stabilize the CubeSat. The thruster-allocation method can stabilize the CubeSat and maintain the pointing to within an error of 3 deg.

The results show that the thruster-allocation method has an advantage over the paired-firing, especially in cases of thruster

failure. The thruster-allocation method can properly distribute the control with the best possible firing combination. Another advantage of the thruster-allocation method is that it works for arbitrary geometries based on different thruster arrangements. The only parameters to be tuned are the values of proportional and derivative gains, whereas paired-firing method only works for the geometry purposed earlier. The thruster-allocation method could also be supplemented with a propellant management scheme that biases the allocation to optimize the distribution of remaining propellant. Such an extension would mitigate the drawback of PPT systems compared to distributed liquid or gaseous propellant systems.



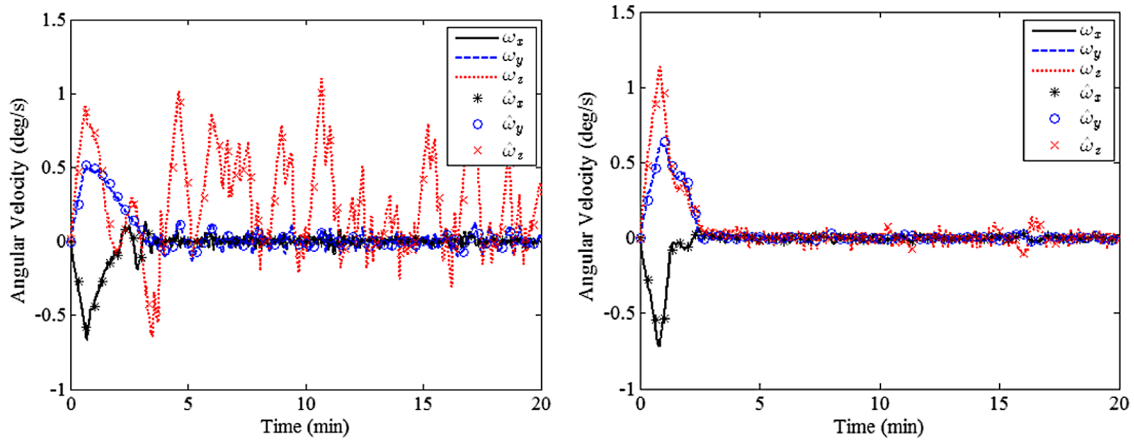


Fig. 29 Angular velocity of a 3U CubeSat using  $\mu$ PPTs with paired firing (left) and thruster allocation (right) assuming two failed thrusters.

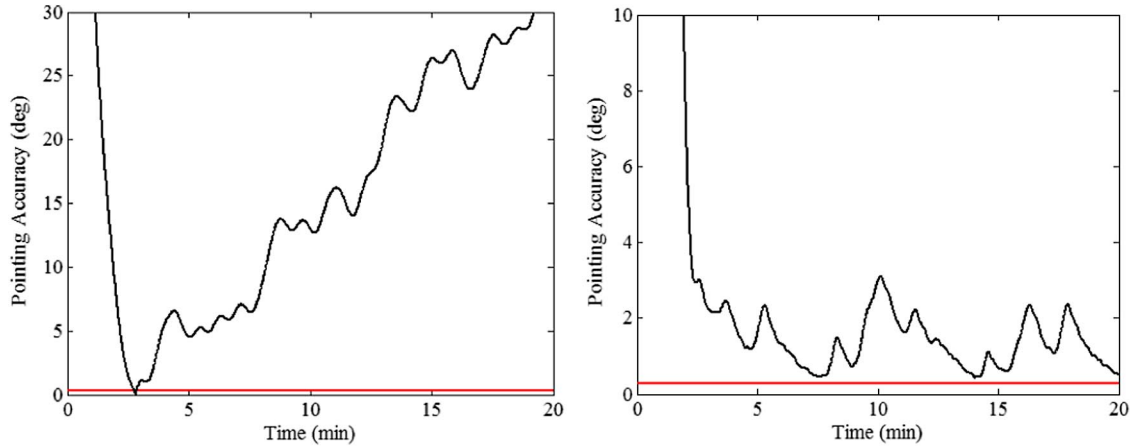


Fig. 30 Pointing angle error of a 3U CubeSat using  $\mu$ PPTs with paired firing (left) and thruster allocation (right) assuming three failed thrusters.

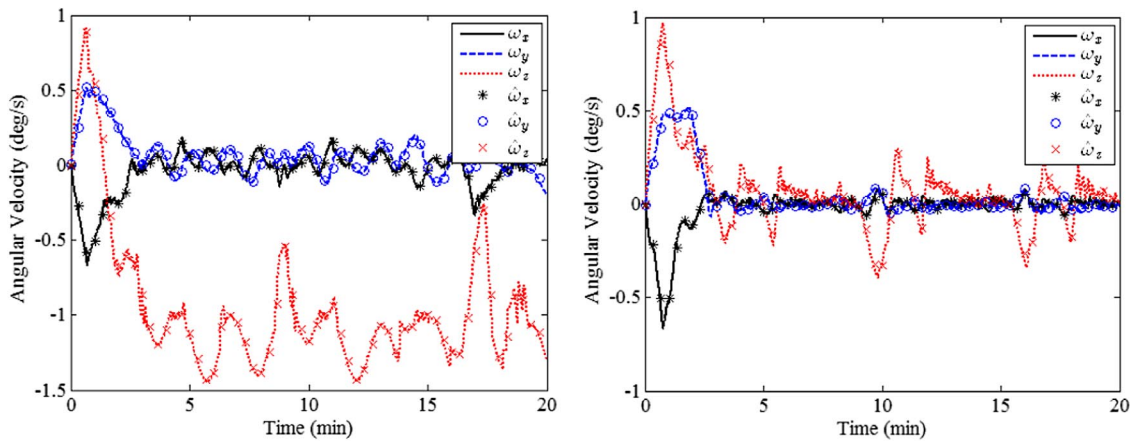


Fig. 31 Angular velocity of a 3U CubeSat using  $\mu$ PPTs with paired firing (left) and thruster allocation (right) assuming three failed thrusters.

## VI. Conclusions

This paper presents a feasibility study for use of a  $\mu$ PPT in attitude control of a 3U CubeSat. The conceptual design includes a  $\mu$ PPT module consisting of eight thrusters occupying 1U of the CubeSat. Sizing of the  $\mu$ PPT and the propulsion module is based on the magnitude of disturbance torques, which will be experienced by the 3U CubeSat in LEO, as well as stabilization and slewing maneuvers. The dynamical model is developed for discrete and continuous time systems, the actuator model, reference models, and control strategies using the  $\mu$ PPT for different mission scenarios: stabilization, pointing, and pointing with spinning. The control approach is implemented in MATLAB and numerical simulations

using a 3U CubeSat equipped with COTS sensors for the three mission scenarios. Results show that the use of the  $\mu$ PPT for attitude control on a CubeSat is feasible, and that it achieves high accuracy in attitude and pointing. The thruster-allocation method is shown to be robust in cases of thruster failure.

## References

- [1] Gatsonis, N. A., Lu, Y., Blandino, J. J., Demetriou, M. A., and Paschalidis, N., "CubeSat Design and Attitude Control with Micro-Pulsed Plasma Thrusters," *AIAA SPACE Forum*, AIAA Paper 2014-4211, 2014.

- [2] Roethlisberger, G., Jordan, F., Servonet, A., Borgeaud, M., Krpoun, R., and Shea, H. R., "Advanced Methods for Structural Machining and Solar Cell Bonding Allowing High System Integration and their Demonstration on a Pico-Satellite," *22nd AIAA/USU Conference on Small Satellites*, AIAA/USU Paper SSC08-XI-4, 2008.
- [3] Visser, F., "A Technical Background of the ZACUBE-i Satellite Mission Series," *11th Annual CubeSat Developers' Workshop — The Edge of Exploration*, April 2014.
- [4] Logan, R., and Greenland, S., "UKube-1: A Multi-Payload Technology Demonstration Platform," *8th Annual CubeSat Developers' Workshop*, California Polytechnic State Univ., San Luis Obispo, CA, April 2011.
- [5] Balan, M., Piso, M., Stoica, A. M., Dragasanu, C. G., Trusculescu, M. F., and Dumitru, C. M., "GOLIAT Space Mission: Earth Observation and Near Earth Environment Monitoring Using Nano-satellites," *59th International Astronautical Congress*, International Astronautical Federation (IAF), Glasgow, Scotland, U.K., Sept.–Oct. 2008.
- [6] Bridges, C. P., Kenyon, S., Underwood, C. I., and Sweeting, M. N., "STRaND: Surrey Training Research and Nanosatellite Demonstrator," *1st IAA Conference on University Satellite Mission and CubeSat Workshop*, 2011.
- [7] Hinkley, D., and Hardy, B., "Picosatellites and Nanosatellites at The Aerospace Corporation," *In-Space Non-Destructive Inspection Technology Workshop*, NASA Johnson Space Center, Houston, TX, Feb.–Mar. 2012.
- [8] Conklin, J. W., et al., "The Drag-Free CubeSat," *26th AIAA/USU Conference on Small Satellites*, AIAA/USU Paper SSC12-VI-8, 2012.
- [9] Jong, S., Aalbers, G. T., and Bouwmeester, J., "Improved Command and Data Handling System for the Delfi-n3Xt Nanosatellite," *59th International Astronautical Congress*, IAF IAC-08.D1.4.11, Glasgow, Scotland, U.K., Sept.–Oct. 2008.
- [10] Sundaramoorthy, P. P., Gillm, E., Verhoeven, C. J. M., and Bouwmeester, J., "Two CubeSats with  $\mu$ -Propulsion in the QB50 Satellite Network," *24th AIAA/USU Conference on Small Satellites*, AIAA/USU Paper SSC10-III-3, 2010.
- [11] Moore, G., et al., "3D Printing and MEMS Propulsion for the RAMPART 2U CUBESAT," *24th AIAA/USU Conference on Small Satellites*, AIAA/USU Paper SSC10-III-8, 2010.
- [12] Shaw, P. V., and Lappas, V. J., "Design, Development and Evaluation of an 8  $\mu$ PPT Propulsion Module for a 3U CubeSat Application," *31st International Electric Propulsion Conference*, IEPC Paper 2011-115, 2011.
- [13] Clark, C., Guarducci, F., Coletti, M., and Gabriel, S. B., "An Off-the-Shelf Electric Propulsion System for CubeSats," *25th Annual AIAA/USU Conference on Small Satellites*, AIAA/USU Paper SSC11-VI-12, 2011.
- [14] Kronhaus, I., Schilling, K., Jayakum, S., Kramer, A., Pietzka, M., and Schein, J., "Design of the UWE-4 Picosatellite Orbit Control System Using Vacuum-Arc-Thrusters for Picosatellites," *33rd International Electric Propulsion Conference*, IEPC Paper 2013-195, 2013.
- [15] Conversano, R. W., and Wirz, R. W., "Mission Capability Assessment of CubeSats Using a Miniature Ion Thruster," *Journal of Spacecraft and Rockets*, Vol. 50, No. 5, 2013, pp. 1035–1046.  
doi:10.2514/1.A32435
- [16] Laperriere, D., Gatsonis, N. A., and Demetriou, M. A., "Electro-mechanical Modeling of Applied Field Micro Pulsed Plasma Thrusters," *41st AIAA/ASME/SAE/ASEE Joint Propulsion Conference and Exhibit*, AIAA Paper 2005-4077, 2005.
- [17] Gatsonis, N. A., Juric, D., and Stechmann, D. P., "Numerical Analysis of Teflon Ablation in Solid Fuel Pulsed Plasma Thrusters," *43rd AIAA/ASME/SAE/ASEE Joint Propulsion Conference*, AIAA Paper 2007-5227, 2007.
- [18] Gatsonis, N. A., Eckman, R., Yin, X., Pencil, E. J., and Myers, R. M., "Experimental Investigations and Numerical Modeling of Pulsed Plasma Thruster Plumes," *Journal of Spacecraft and Rockets*, Vol. 38, No. 3, May–June 2001, pp. 454–464.  
doi:10.2514/2.3704
- [19] Wie, B., *Space Vehicle Dynamics and Control*, 2nd ed., AIAA Education Series, AIAA, Reston, VA, 2008, Chaps. 5–7.
- [20] Wertz, J. R., *Spacecraft Attitude Determination and Control*, Kluwer Academic, Boston, 1980, Chaps. 12–18.
- [21] Markley, F. L., and Crassidis, J. L., *Fundamentals of Spacecraft Attitude Determination and Control*, Space Technology Library, Springer, New York, 2015, Chaps. 5, 7.
- [22] Sidi, M. J., *Spacecraft Dynamics and Control: A Practical Engineering Approach*, Cambridge Univ. Press, Cambridge, England, U.K., 2000, pp. 265–173.
- [23] Billings, D., Graedel, I., Hoey, F., Lavallee, P., Martinez, N., and Torres, J., "Design and Analysis for a CubeSat Mission," Worcester Polytechnic Inst., Major Qualifying Project Rept. NAG-1204, Worcester, MA, 2013.
- [24] Farhat, A. T., Ivase, J. T., Lu, Y., and Snapp, A. T., "Attitude Determination and Control System for CubeSat," Worcester Polytechnic Inst., Major Qualifying Project Rept. MAD-1301, Worcester, MA, 2013.
- [25] Hanley, J. M., Joseph, B. J., Miller, M. O., Monte, S. J., Trudeau, J. R., and Weinrick, R. L., "Thermal, Telecommunication and Power Systems for a CubeSat," Worcester Polytechnic Inst., Major Qualifying Project Rept. JB3-CBS3, Worcester, MA, 2013.
- [26] Eslava, S., Marchetto, J., and Scougal, E., "Design of a Micro-Pulsed Plasma Thruster for a 3U CubeSat," Worcester Polytechnic Inst., Major Qualifying Project Rept. NAG-1302, Worcester, MA, 2014.
- [27] Wertz, J. R., and Larson, W. J., *Space Mission Analysis and Design*, 3rd ed., Space Technology Library, New York, 2008, Chap. 11.
- [28] Systems Tool Kit, Software Package, Ver. 9.0.1, Analytical Graphics, Inc., Kluwer Academic Publ., Microcosm Press, Exton, PA, 2013.
- [29] Wahba, G., "A Least Squares Estimate of Spacecraft Attitude," *SIAM Review*, Vol. 7, No. 3, 1965, p. 409.  
doi:10.1137/1007077
- [30] The Astronomical Almanac 2010: Data for Astronomy, Space Sciences, Geodesy, Surveying, Navigation and Other Applications, United Kingdom Hydrographic Office, Taunton, England, U.K., 2010.
- [31] Finlay, C. C., et al., "International Geomagnetic Reference Field: the eleventh generation," *Geophysical Journal International*, Vol. 183, No. 3, Dec. 2010, pp. 1216–1230.  
doi:10.1111/j.1365-246X.2010.04804.x
- [32] Winch, D. E., Ivers, D. J., Turner, J. P. R., and Stening, R. J., "Geomagnetism and Schmidt Quasi-Normalization," *Geophysical Journal International*, Vol. 160, No. 2, Feb. 2005, pp. 487–504.  
doi:10.1111/gji.2005.160.issue-2
- [33] Oppenheimer, M. W., and Doman, D. B., "Thruster Allocation for Over-Actuated Systems," U.S. Air Force Research Lab., AFRL-VA-WP-TP-2006-321, April 2006.
- [34] Murray, W., and Ng, K. M., "An Algorithm for Nonlinear Optimization Problems with Binary Variables," *Computational Optimization and Applications*, Vol. 47, No. 2, Oct. 2010, pp. 257–288.  
doi:10.1007/s10589-008-9218-1
- [35] MATLAB, Software Package, Ver. 7.14.0.739 (R2012a), The MathWorks, Inc, Natick, MA, 2014.
- [36] Grewal, S. M., and Andrews, P. A., *Kalman Filtering: Theory and Practice Using Matlab*, 3rd ed., Wiley-IEEE Press, Piscataway, NJ, 2008, Chaps. 4, 6.

M. Walker  
Associate Editor